

## **Quarterly Technical Report**

## **Solid State Research**

**2005:1**

---

**Lincoln Laboratory**  
MASSACHUSETTS INSTITUTE OF TECHNOLOGY  
*LEXINGTON, MASSACHUSETTS*



---

Prepared for the Department of the Air Force under Contract F19628-00-C-0002.

Approved for public release; distribution is unlimited.



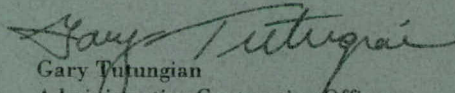
This report is based on studies performed at Lincoln Laboratory, a center for research operated by Massachusetts Institute of Technology. This work was sponsored by the Department of the Air Force under Contract F19628-00-C-0002.

This report may be reproduced to satisfy needs of U.S. Government agencies.

The ESC Public Affairs Office has reviewed this report, and it is releasable to the National Technical Information Service, where it will be available to the general public, including foreign nationals.

This technical report has been reviewed and is approved for publication.

FOR THE COMMANDER

  
Gary Tutungian  
Administrative Contracting Officer  
Plans and Programs Directorate  
Contracted Support Management

Non-Lincoln Recipients

PLEASE DO NOT RETURN

Permission is given to destroy this document  
when it is no longer needed.

Massachusetts Institute of Technology  
Lincoln Laboratory

**Solid State Research**

Quarterly Technical Report  
2005:1

1 November 2004 – 31 January 2005

Issued 21 June 2005

Approved for public release; distribution is unlimited.

## **ABSTRACT**

This report covers in detail the research work of the Solid State Division at Lincoln Laboratory for the period 1 November 2004 through 31 January 2005. The topics covered are Quantum Electronics, Electro-optical Materials and Devices, Submicrometer Technology, Biosensor and Molecular Technologies, Advanced Imaging Technology, Analog Device Technology, and Advanced Silicon Technology. Funding is provided by several DoD organizations—including the Air Force, Army, DARPA, MDA, Navy, NSA, and OSD—and also by the DOE, NASA, and NIST.



## TABLE OF CONTENTS

Abstract	iii
List of Illustrations	vii
List of Tables	xi
Introduction	xiii
Reports on Solid State Research	xv
Organization	xxiii
 1. QUANTUM ELECTRONICS	
1.1 Fluorescence-Cued Laser-Induced Breakdown Spectroscopy Detection of Bioaerosols	1
 2. ELECTRO-OPTICAL MATERIALS AND DEVICES	
2.1 Narrow-Linewidth, High-Power 1556-nm Slab-Coupled Optical Waveguide External-Cavity Laser	7
 3. SUBMICROMETER TECHNOLOGY	
3.1 A Variable-Transmittance Apodizing Filter at 157 nm	13
3.2 Field Emission at $10 \text{ V cm}^{-1}$ with Surface Emission Cathodes on Negative Electron Affinity Insulators	17
 4. BIOSENSOR AND MOLECULAR TECHNOLOGIES	
4.1 Testing of the Affinity Magnet Cartridge	23
 5. ADVANCED IMAGING TECHNOLOGY	
5.1 High-Fill-Factor Silicon Geiger-Mode Avalanche Photodiode Arrays for Photon-Counting Applications	29

6. ANALOG DEVICE TECHNOLOGY

6.1 Intermodulation Distortion in High-Temperature Superconductor Filters	35
---------------------------------------------------------------------------	----

7. ADVANCED SILICON TECHNOLOGY

7.1 Megapixel CMOS Image Sensor Fabricated in Three-Dimensional Integrated Circuit Technology	39
-----------------------------------------------------------------------------------------------	----



## LIST OF ILLUSTRATIONS

Figure No.		Page
1-1	Conceptual schematic of fluorescence-cued laser-induced breakdown spectroscopy (LIBS) instrument.	2
1-2	Representative single-particle spectra of five types of simulants. Included in each spectrum is the mean particle diameter $d_p$ of the aerosol used for each measurement. All samples were washed once with deionized water to remove the saline buffer used in the production of lyophilized samples. Since LIBS measurements are limited by signal-to-background ratio, rather than absolute signal strength, the spectra are plotted in units of signal divided by background; therefore, areas of the spectrum with no signal from the particle have a ratio of 1.	3
1-3	(a) Time series of concurrent Biological Agent Warning Sensor (BAWS) and LIBS measurements of outdoor aerosol. From top to bottom, plots show BAWS “toxin” counts as a function of time; LIBS sensor measurements of toxin-like particles (by fluorescence signature only); the number of particles containing Ca, Na, and K; and the number of particles that appear toxin-like when both the elemental information and fluorescence signatures are utilized. (b) Similar time series for Bg-like particles.	4
2-1	Equipment configuration for gain spectra measurements of curved-channel slab-coupled optical waveguide amplifier (SCOWA). Top view and cross section of the SCOWA device are also shown.	8
2-2	Measured double-pass fiber-coupled gain spectra of curved-channel SCOWA. Tunable-laser wavelength step $\Delta\lambda = 1$ nm.	9
2-3	SCOW external-cavity laser (SCOWECL) comprising a curved-channel SCOWA gain section, fiber Bragg grating, and output isolator. The laser characterization setup is also shown.	10
2-4	Self-heterodyne linewidth measurement of SCOWECL operating with 88-mW output power. Both Lorentzian (dash) and Gaussian (dash-dot) fits are shown.	10
3-1	Schematic drawing of experimental test bed for apodizer.	14

## LIST OF ILLUSTRATIONS (Continued)

Figure No.		Page
3-2	Intensity map through flood-exposed apodizer cell at different levels of oxygen. Each solid trace represents a separate x or y directional scan. The dashed curves represent the theoretical intensity maps. In order to match the position of the diffraction nulls, the Airy distribution for a 65- $\mu\text{m}$ , rather than 75- $\mu\text{m}$ , pinhole has been used in computing the theoretical curves.	15
3-3	Intensity map in image plane with 1-atm $\text{N}_2$ and 2-atm $\text{O}_2$ flowing through the apodizing cell. The dashed curves represent the theoretical profiles.	16
3-4	Surface emission glass cathode: (a) Optical micrograph of two metal electrodes on a glass-silicon substrate, and (b) schematic cross section of the cathode for the region marked with yellow arrows in (a). The electrodes seen on the left and right sides of (b) are fabricated with a tungsten/aluminum structure that is undercut to form a submicrometer gap between the tungsten layer and the glass surface.	18
3-5	Schematic cross section of cathode indicating the distribution of charge and electric field as one electrode is biased to 200 V and then grounded, with the other electrode and the silicon substrate both grounded. Diagrams illustrate cathode (a) under initial testing, (b) after several minutes to several hours of operation, and (c) after bias voltage is removed.	19
3-6	(a) Electrical properties of one of the better cathodes during its first testing, with the inset showing bias voltage and bias current as a function of time. The bias current remains negative after the bias voltage was decreased. (b) Anode current as a function of anode voltage and surface electric field into vacuum. After emission is initiated with a bias voltage of $\sim 200$ V, the bias voltage is held at 0 V and the anode voltage is swept from 200 to $-200$ V.	20



## LIST OF ILLUSTRATIONS (Continued)

Figure No.		Page
4-1	Detection of Ba spores seeded into dirty water using the Affinity Magnet (AM) cartridge protocol with a sample volume of 5 mL, a magnetic bead mass of 25 mg, a 10-sphere chain of collection magnets in the processing chamber, and a magnetic bead collection time of 1 min. Detection from eluate is observed down to 10 spores/mL compared to 100 spores/mL with no concentration. Note that eluate curves show reduced spurious background fluorescence that is commonly present in this type of sample, indicating that the AM concentration step has also eliminated most of the polymerase chain reaction (PCR) interferences. Also shown is the level of unconcentrated target left behind in the supernatant (blue curves).	24
4-2	Detection of Ba spores seeded into sand using the AM cartridge protocol with a sample volume of 1 g of sand with 5 mL of distilled water, a magnetic bead mass of 15 mg, a two-cylinder-stack collection magnet in the processing chamber, and a magnetic bead collection time of 1 min. Detection from eluate is observed down to 100 spores/mL, compared to 1000 spores/mL with no concentration.	25
4-3	Detection of Ba vegetative cells seeded into dirty water using the AM cartridge protocol with a sample volume of 5 mL of liquid, a magnetic bead mass of 15 mg, a two-cylinder-stack collection magnet in the processing chamber, and a magnetic bead collection time of 1 min. Detection from eluate is observed down to 10 cells/mL, compared to no detection at all with unprocessed samples.	26
4-4	Detection of Ba vegetative cells seeded into sand using the AM cartridge protocol with a sample volume of 1 g of sand in 5 mL of distilled water, a magnetic bead mass of 15 mg, a two-cylinder-stack collection magnet in the processing chamber, and a magnetic bead collection time of 1 min. Detection is observed down to seeding levels of 1000 spores/mL at an earlier cycle threshold than with unprocessed samples. Note that this seeding level was the lowest tested in this experiment; we expect the limit of detection to be lower when lower levels are tested.	27
5-1	Cartoon cross section of traditional low-fill-factor Geiger-mode avalanche photodiode (GM-APD) showing avalanche region and guard ring.	30

## LIST OF ILLUSTRATIONS (Continued)

Figure No.		Page
5-2	Cartoon cross section of high-fill-factor GM-APD showing avalanche region and guard ring.	30
5-3	Process sequence to create high-fill-factor GM-APDs using a stepped $p^+$ buried layer.	31
5-4	Breakdown and punchthrough values for GM-APD device at an implant dose of $2.7 \times 10^{12} \text{ cm}^{-2}$ , showing punchthrough before breakdown, low initiation probability, and high collection efficiency.	32
5-5	Breakdown and punchthrough values for GM-APD device at an implant dose of $2.9 \times 10^{12} \text{ cm}^{-2}$ , showing breakdown before punchthrough resulting in a higher initiation probability and lower collection efficiency than in Figure 5-4.	33
6-1	Equivalent circuit of a resonator. $R(I)$ and $L(I)$ are from Equations (6.1) and (6.2), where $R_0$ , $L_0$ , and $C$ are given by the transmission line parameters [1]. $C_c$ is the coupling capacitor, and $R_g = R_L = 50 \Omega$ are the load and source impedances. The resonator $Q$ is given by $R/\omega L$ .	36
6-2	Measured and calculated intermodulation distortion (IMD) for YBCO resonator at $T = 50 \text{ K}$ . Solid lines are calculations, open circles are the measured fundamental frequency, and open squares are the measured third-order IMD.	36
6-3	Frequency response of five-pole filter and position of input tones for the intermodulation calculation. The frequencies are 2.0095 and 2.0105 GHz, chosen to be centered at the edge of the passband.	36
6-4	Results of the intermodulation calculation. Circles are the output at fundamental frequencies, and triangles are the output at intermodulation frequencies.	37
7-1	Schematic diagram of three-dimensional (3-D) stacked imager circuit. Tier 1 is a silicon photodetector wafer, and tier 2 is an inverted fully depleted silicon-on-insulator (FDSOI) CMOS wafer.	40
7-2	Cross-sectional scanning electron micrograph through a functional active pixel imager.	40



## LIST OF ILLUSTRATIONS (Continued)

Figure No.		Page
7-3	Schematic of a pixel of the $1024 \times 1024$ array. Each pixel includes a reverse-biased $p^+/n$ diode (in tier 1) and a reset transistor, source follower transistor, and select transistor (in tier 2).	41
7-4	Photographs of (a) completed 3-D integrated 150-mm wafer pair and (b) $22 \times 22$ -mm die after integration.	42
7-5	Block diagram of 3-D integrated image sensor.	42
7-6	Sample image from the $1024 \times 1024$ -pixel array.	43

## LIST OF TABLES

Table No.		Page
4-1	Summary of Preliminary Test Results for COTS-Based AM Cartridge	27

## INTRODUCTION

### 1. QUANTUM ELECTRONICS

A transportable fluorescence-cued laser-induced breakdown spectroscopy (LIBS) sensor has been developed to measure the elemental content of fluorescent, naturally occurring aerosol particles. The elemental signatures of the outdoor aerosols were compared to those of bioagent simulants in order to assess the discrimination capability of LIBS for bioaerosol detection.

### 2. ELECTRO-OPTICAL MATERIALS AND DEVICES

An external-cavity laser has been demonstrated comprising a novel InGaAsP/InP curved-channel slab-coupled optical waveguide amplifier and a fiber Bragg grating. The laser exhibits a technical-noise-limited linewidth of 130 kHz with 88-mW output power at 1556 nm.

### 3. SUBMICROMETER TECHNOLOGY

A variable-transmittance apodizing filter has been designed and demonstrated at 157 nm. The Gaussian transmission function is created by flowing oxygen gas, which is absorptive below 185 nm, between the two spherical surfaces of meniscus lenses.

Electron emission, with fields as low as  $10 \text{ V cm}^{-1}$ , was achieved with a surface emission cathode formed on a cesium-doped glass substrate, which is a negative electron affinity insulator. For some cathodes, emission continues after the gate bias is removed and for anode voltages as low as 20 V.

### 4. BIOSENSOR AND MOLECULAR TECHNOLOGIES

Use of the Affinity Magnet cartridge has enabled detection of washed Ba spores to 10 spores/mL of dirty environmental water and 100 spores/mL of sand, in both cases a factor of 10 better than obtained with unprocessed samples. In addition, Ba vegetative cells were detected at 10 cells/mL of dirty water and at 1000 cells/mL of sand (the lowest level tested so far).

### 5. ADVANCED IMAGING TECHNOLOGY

Early results on high-fill-factor silicon Geiger-mode avalanche photodiode (APD) designs have shown promise, with successful demonstration of breakdown and punchthrough characteristics. These detectors will increase the range of applications in the growing field of single-photon-sensitive APDs.

### 6. ANALOG DEVICE TECHNOLOGY

The intermodulation distortion (IMD) in a resonator has been successfully modeled using the nonlinear surface impedance  $Z_S$ . The modeling has also been extended to a resonator-coupled filter.



## 7. ADVANCED SILICON TECHNOLOGY

A three-dimensional (3-D) integrated  $1024 \times 1024$ ,  $8\text{-}\mu\text{m}$ -pixel visible image sensor has been fabricated using oxide-to-oxide wafer bonding and  $2\text{-}\mu\text{m}$ -square 3-D vias in every pixel. The 150-mm wafer technology integrates a low-leakage, deep-depletion, 100% fill factor photodiode layer to a 3.3-V,  $0.35\text{-}\mu\text{m}$ -gate-length, fully depleted silicon-on-insulator CMOS readout circuit layer.

# REPORTS ON SOLID STATE RESEARCH

## 1 NOVEMBER 2004 THROUGH 31 JANUARY 2005

### PUBLICATIONS

A Variable-Transmittance Apodizing Filter at 157 nm	T. M. Bloomstein D. E. Hardy M. Rothschild	<i>Opt. Express</i> <b>13</b> , 648 (2005)
CCD Soft-X-Ray Detectors with Improved High- and Low-Energy Performance	B. E. Burke J. A. Gregory A. H. Loomis M. Lesser* M. W. Bautz* S. E. Kissel* D. D. Rathman R. M. Osgood M. J. Cooper T. A. Lind G. R. Ricker*	<i>IEEE Trans. Nucl. Sci.</i> <b>51</b> , 2322 (2004)
Submicrosecond Submilliwatt Silicon-on-Insulator Thermooptic Switch	M. W. Geis S. J. Spector R. C. Williamson T. M. Lyszczarz	<i>IEEE Photonics Technol. Lett.</i> <b>16</b> , 2514 (2004)
Ohmic Contacts to <i>n</i> -Type GaSb and <i>n</i> -Type GaInAsSb	R. K. Huang C. A. Wang C. T. Harris M. K. Connors D. A. Shiau*	<i>J. Electron. Mater.</i> <b>33</b> , 1406 (2004)

---

\*Author not at Lincoln Laboratory.



Auger and Radiative  
Recombination Coefficients  
in 0.55-eV InGaAsSb

R. J. Kuman\*  
J. M. Borrego\*  
P. S. Dutta\*  
R. J. Gutmann\*  
C. A. Wang  
G. Nichols\*

*J. Appl. Phys.* **97**, 023530-1  
(2005)

Quantum and Transport Lifetimes  
in a Tunable Low-Density AlGaIn/  
GaIn Two-Dimensional Electron  
Gas

M. J. Manfra  
S. H. Simon\*  
K. W. Baldwin\*  
A. M. Sergent\*  
K. W. West\*  
R. J. Molnar  
J. M. Caissie

*Appl. Phys. Lett.* **85**, 5278  
(2004)

Observations of the Nonlinear  
Meissner Effect in YBCO Thin  
Films: Evidence for a d-Wave  
Order Parameter in the Bulk of the  
Cuprate Superconductors

D. E. Oates  
S.-H. Park  
G. Koren\*

*Phys. Rev. Lett.* **93**, 197001-1  
(2004)

Micro-Auger Electron  
Spectroscopy Studies of Chemical  
and Electronic Effects at GaIn-  
Sapphire Interfaces

X. L. Sun\*  
S. T. Bradley\*  
G. H. Jessen\*  
D. C. Look\*  
R. J. Molnar  
L. J. Brillson\*

*J. Vac. Sci. Technol. A* **22**, 2284  
(2004)

IV-VI Device Arrays:  
Microfabrication and Specific  
Contact Resistivity

P. J. Taylor  
T. C. Harman  
N. K. Dhar\*  
P. S. Wijewarnasuriya\*  
J. C. Fraser\*  
M. Z. Tidrow\*

*Appl. Phys. Lett.* **85**, 5415  
(2004)

---

\*Author not at Lincoln Laboratory.

Effect of Growth Interruption on  
Surface Recombination Velocity in  
GaInAsSb/AlGaAsSb  
Heterostructures Grown by  
Organometallic Vapor-Phase  
Epitaxy

C. A. Wang  
D. A. Shiau\*  
S. Anikeev\*  
G. Belenky\*  
S. Luryi\*

*J. Cryst. Growth* **272**, 711  
(2004)

# PRESENTATIONS<sup>†</sup>

Wavelength Beam Combining of  
Slab-Coupled Optical Waveguide  
Laser (SCOWL) Arrays

B. Chann  
R. K. Huang  
L. J. Missaggia  
C. T. Harris  
Z. L. Liao  
A. K. Goyal  
J. P. Donnelly  
T. Y. Fan  
A. Sanchez  
G. W. Turner

17th Annual Meeting of the  
IEEE Lasers and Electro-Optics  
Society,  
Rio Mar, Puerto Rico,  
7-11 November 2004

Simple Derivation of Four-Level  
Permittivity Relations for Magneto-  
Optical Applications

G. F. Dionne

49th Annual Conference on  
Magnetism and Magnetic  
Materials,  
Jacksonville, Florida,  
7-11 November 2004

Ferrite Properties and Technology  
Issues for Improved Microwave  
Systems (Invited)

G. F. Dionne

Fall Meeting of the Materials  
Research Society,  
Boston, Massachusetts,  
29 November–  
3 December 2004

The Development of Immersion  
Lithography

M. Switkes  
M. Rothschild

Fall Meeting of the Materials  
Research Society,  
Boston, Massachusetts,  
29 November–  
3 December 2004

\*Author not at Lincoln Laboratory.

<sup>†</sup> Titles of presentations are listed for information only. No copies are available for distribution.

Laser-Based Precision Oscillators	S. J. Augst J. J. Hargreaves J. C. Twichell T. Y. Fan	DARPA Microsystems Technology Office (MTO) Photonics Symposium, San Francisco, California, 30 November– 2 December 2004
Semiconductor UV Optical Sources (SUVOS) Biological Agent Sensor Testbed	T. H. Jeys A. J. Angell* R. H. Hoffeld J. G. Ingwersen N. M. F. Judson X. L. Eapen T. F. Lunny G. C. Molnar M. Nischan V. Daneu	DARPA Microsystems Technology Office (MTO) Photonics Symposium, San Francisco, California, 30 November– 2 December 2004
Thermophoretic Preconcentrator	M. W. Geis S. J. Spector T. M. Lyszcza	Bio-Chem Defense Workshop, Lincoln Laboratory, Lexington, Massachusetts, 1-2 December 2004
CANARY Bio-Identifier Developments	J. Harper	Bio-Chem Defense Workshop, Lincoln Laboratory, Lexington, Massachusetts, 1-2 December 2004
Bioparticle Surface Imaging System	W. D. Herzog	Bio-Chem Defense Workshop, Lincoln Laboratory, Lexington, Massachusetts, 1-2 December 2004
LIBS for Bio-Aerosol Detection with Improved Clutter Rejection	J. D. Hybl S. M. Tysk M. P. Jordan	Bio-Chem Defense Workshop, Lincoln Laboratory, Lexington, Massachusetts, 1-2 December 2004

---

\*Author not at Lincoln Laboratory.



Biological Agent Sensor Testbed (BAST)	T. H. Jeys	Bio-Chem Defense Workshop, Lincoln Laboratory, Lexington, Massachusetts, 1-2 December 2004
Chemical Sensing: Status and Future Prospects	R. R. Kunz	Bio-Chem Defense Workshop, Lincoln Laboratory, Lexington, Massachusetts, 1-2 December 2004
Single-Particle Ion Mobility Spectrometry for Bio-Aerosol Detection	R. R. Kunz	Bio-Chem Defense Workshop, Lincoln Laboratory, Lexington, Massachusetts, 1-2 December 2004
Electrokinetic Particle Manipulation Methods for CANARY	L. Parameswaran C. Cabrera M. Angel	Bio-Chem Defense Workshop, Lincoln Laboratory, Lexington, Massachusetts, 1-2 December 2004
PANACEA Broad-Spectrum Antimicrobials	T. Rider	Bio-Chem Defense Workshop, Lincoln Laboratory, Lexington, Massachusetts, 1-2 December 2004
B-Cell Detection of DNA Sequences	E. Schwoebel	Bio-Chem Defense Workshop, Lincoln Laboratory, Lexington, Massachusetts, 1-2 December 2004
Curving Silicon CCD Detectors to a Spherical Focal Surface	J. A. Gregory A. H. Loomis B. B. Kosicki	IEEE International Electron Devices Meeting, San Francisco, California, 12-15 December 2004
Nanostructured Thermoelectric Materials	T. C. Harmon R. E. Reeder M. P. Walsh B. E. LaForge C. D. Hoyt	Direct Energy Conversion Program Review and Workshop, Coronado, California, 13-15 December 2004

Rapid Detection of Bacteria in Food  
with the CANARY B-Cell Sensor

J. Harper  
M. Petrovick

Food Safety Workshop,  
Boston, Massachusetts,  
14 December 2004

CMOS Microphotonics Fabrication

S. J. Spector  
T. M. Lyszczarz  
M. W. Geis  
J. Yoon  
D. M. Lennon

DARPA Electronic and  
Photonic Integrated Circuits  
(EPIC) Kick-Off Meeting,  
Arlington, Virginia,  
16-17 December 2004

All-Optical Hybrid Maskless  
Lithography for Sub-45 nm

M. Rothschild  
M. Fritze  
T. M. Bloomstein  
B. Tyrrell  
T. H. Fedynyshyn  
N. N. Efremow  
D. E. Hardy

Maskless Lithography  
Workshop,  
Chicago, Illinois,  
17-20 January 2005

Thermo-Optic Properties of Laser  
Crystals in the 100–300 K  
Temperature Range:  
 $\text{Y}_3\text{Al}_5\text{O}_{12}$  (YAG),  $\text{YAlO}_3$  (YALO)  
and  $\text{LiYF}_4$  (YLF)

R. L. Aggarwal  
D. R. Ripin  
J. R. Ochoa  
T. Y. Fan

SPIE Photonics West,  
San Jose, California,  
22-27 January 2005

Coherent (Phased Array) and  
Wavelength (Spectral) Beam  
Combining Compared

T. Y. Fan  
A. Sanchez

SPIE Photonics West,  
San Jose, California,  
22-27 January 2005

150-W Cryogenically Cooled  
Yb:YAG Laser

D. J. Ripin  
J. R. Ochoa  
R. L. Aggarwal  
T. Y. Fan

SPIE Photonics West,  
San Jose, California,  
22-27 January 2005

The Development of Immersion  
Lithography

M. Switkes  
M. Rothschild

Technical Seminar,  
Cabot Corporation,  
Billerica, Massachusetts,  
25 January 2005

Generating Electric Power with a  
MEMS Electroquasistatic Induction  
Turbine-Generator

J. L. Steyn\*  
S. H. Kendig\*  
R. Khanna\*  
T. M. Lyszczarz  
S. D. Umans\*  
J. U. Yoon  
C. Livermore\*  
J. H. Lang\*

18th International Conference  
on Micro Electro Mechanical  
Systems,  
Miami, Florida,  
30 January–3 February 2005

---

\*Author not at Lincoln Laboratory.



## ORGANIZATION

### SOLID STATE DIVISION

D. C. Shaver, Head  
R. W. Ralston, Associate Head  
N. L. DeMeo, Jr., Assistant  
Z. J. Lemnios, Senior Staff  
K. J. Challberg, Administrative Staff  
L. K. Pacheco, Administrative Staff  
J. D. Pendergast, Administrative Staff

#### SUBMICROMETER TECHNOLOGY

M. Rothschild, Leader  
T. M. Lyszczarz, Assistant Leader  
T. H. Fedynyshyn, Senior Staff  
R. R. Kunz, Senior Staff

Astolfi, D. K.  
Bloomstein, T. M.  
Cann, S. G.  
Efremow, N. N., Jr.  
Geis, M. W.  
Goodman, R. B.  
Krohn, K. E.  
Leibowitz, F. L.  
Lennon, D. M.

Lieberman, V.  
Palmacci, S. T.  
Pottebaum, I. S.  
Sedlacek, J. H. C.  
Spector, S. J.  
Switkes, M.  
Wynn, C. M.  
Yoon, J. U.

#### QUANTUM ELECTRONICS

A. Sanchez-Rubio, Leader  
T. Y. Fan, Assistant Leader  
T. H. Jeys, Senior Staff  
J. J. Zayhowski, Senior Staff

Aggarwal, R. L.  
Augst, S. J.  
Chann, B.  
Daneu, J. L.  
DiNatale, W. F.  
Eapen, X. L.  
Goyal, A. K.  
Herzog, W. D.

Hybl, J. D.  
Lynch, E. J.  
O'Brien, P. W.  
Ochoa, J. R.  
Ranka, J. K.  
Ripin, D. J.  
Tysk, S. M.

#### ELECTRO-OPTICAL MATERIALS AND DEVICES

J. C. Twichell, Leader  
G. W. Turner, Assistant Leader  
S. Verghese, Assistant Leader  
J. P. Donnelly, Senior Staff; D. L. Spears, Senior Staff  
C. A. Wang, Senior Staff; R. C. Williamson, Senior Staff

Bailey, R. J.  
Calawa, D. R.  
Calawa, S. D.  
Connors, M. K.  
Duerr, E. K.  
Goodhue, W. D.  
Groves, S. H.  
Hargreaves, J. J.  
Harman, T. C.  
Harris, C. T.  
Huang, R. K.

Jensen, K. E.  
Juodawlkis, P. W.  
LaForge, B. E.  
Liau, Z. L.  
Mahan, J. M.  
Mahoney, L. J.  
Manfra, M. J.  
McIntosh, K. A.  
McNulty, D. D.  
Missaggia, L. J.

Molnar, R. J.  
Mull, D. E.  
Napoleone, A.  
Nitishin, P. M.  
Oakley, D. C.  
O'Donnell, F. J.  
Plant, J. J.  
Smith, G. M.  
Swint, R. B.  
Younger, R. D.

BIOSENSOR AND MOLECULAR  
TECHNOLOGIES

M. A. Hollis, Leader  
T. H. Rider, Senior Staff

Bohane, M. D.	Petrovick, M. S.
Cabrera, C. R.	Riley, M. M.
Graves, C. A.	Schmidt, T. L.
Harper, J. D.	Schwoebel, E. D.
Hogan, K. E.	Theriault, K. A.
Lacirignola, J. J.	Towle, T. A.
Mathews, R. H.	Wick, S. T.
Nargi, F. E.	Zook, C. E.
Pancoast, J. S.	Zusman, B. D.
Parameswaran, L.	

ANALOG DEVICE TECHNOLOGY

M. A. Gouker, Leader  
L. M. Johnson, Assistant Leader

Aversa, J. C.	Murphy, P. G.
Bolkhovsky, V.	Oates, D. E.
Drangmeister, R. G.	Oliver, W. D.
Fitch, G. L.	Sage, J. P.
Hancock, T. M.	Santiago, D. D.
Ieni, S.	Slattery, R. L.
Lyons, W. G.	Straayer, M. Z.
Macedo, E. M., Jr.	Weir, T. J.
Messier, A. V.	

ADVANCED IMAGING TECHNOLOGY

R. K. Reich, Leader  
B. B. Kosicki, Associate Leader  
J. A. Gregory, Assistant Leader  
B. E. Burke, Senior Staff

Aull, B. F.	Loomis, A. H.
Ciampi, J. S.	McGonagle, W. H.
Cooper, M. J.	O'Mara, D. M.
Craig, D. M.	Osgood, R. M.
Daniels, P. J.	Percival, K. A.
Doherty, C. L., Jr.	Rathman, D. D.
Doherty, P. E.	Renzi, M. J.
Dolat, V. S.	Rose, M. K.
Felton, B. J.	Ruth, W. M.
Johnson, K. F.	Stevenson, C. N.
Lambert, R. D.	Young, D. J.
Lind, T. A.	

ADVANCED SILICON TECHNOLOGY

C. L. Keast, Leader  
V. Suntharalingam, Assistant Leader  
P. W. Wyatt, Senior Staff

Austin, E. E.	Hu, W.
Berger, R.	Knecht, J. M.
Bozler, C. O.	Muldavin, J. B.
Brunelle, M. R.	Newcomb, K. L.
Burns, J. A.	Rabe, S.
Chen, C. K.	Soares, A. M.
Chen, C. L.	Tyrrell, B. M.
D'Onofrio, R. P.	Warner, K.
Fritze, M.	Wheeler, B. D.
Gouker, P. M.	Wlodarczak, T. J.
Healey, P. D.	Yost, D.-R.
Healey, R. E.	Young, G. R.

# 1. QUANTUM ELECTRONICS

## 1.1 FLUORESCENCE-CUED LASER-INDUCED BREAKDOWN SPECTROSCOPY DETECTION OF BIOAEROSOLS

Achieving optimal false-alarm rates and classification capabilities with rapid bioaerosol detectors will likely require the fusion of multiple, orthogonal measurement technologies. Combination of elemental analysis with fluorescent particle detection is one example of such a fusion of techniques. Fluorescent particle detectors have proven capability for rapidly detecting bioaerosols and discriminating them against most inorganic aerosols such as dirt and sand. However, other fluorescent materials in the environment, such as combustion by-products and naturally occurring organisms, contribute to clutter. Since biological organisms contain a wide variety of readily detectable inorganic elements, such as Ca, Mg, Mn, Fe, P, Na, K, and Si [1], detection of these elements could improve discrimination against nonbiological, fluorescent aerosols and potentially against classes of naturally occurring organisms such as fungal spores.

Laser-induced breakdown spectroscopy (LIBS) is a practical means for bringing elemental analysis of aerosol particles to the field [2]. The technique involves tightly focusing a laser pulse to create a microplasma via laser breakdown of the aerosol particle or ambient air. Material inside the plasma is ionized and decomposed into atomic constituents. The hot plasma (10,000–15,000 K) provides a thermal excitation source for the atomized species within the plasma volume. Emission from these electronically excited atoms is spectrally resolved and used to determine the elemental composition of the sample. Thus, the orthogonal discrimination capability of LIBS is advantageously combined with the rapid, high-throughput screening of particles by laser-induced fluorescence.

Figure 1-1 is a conceptual schematic of the fluorescence-cued LIBS aerosol sensor. A collimated stream of aerosol particles enters the sample chamber. Individual particles are first illuminated with a 266-nm, 1- $\mu$ J, 500-ps laser pulse from a frequency-quadrupled Nd:YAG microchip laser operating at 10 kHz. Fluorescence and elastic scattering from the particles are collected with an  $f/2$  lens and imaged through a spatial filter. The elastic scatter is separated from the fluorescence by a dichroic beamsplitter (HR-coated WG295 filter) and detected with two 1-inch-square photomultiplier tubes (PMTs). The signal from the fluorescence PMT is sent to a threshold trigger. If the signal exceeds a preset level, indicating the presence of a fluorescent particle, the LIBS laser (actively  $Q$ -switched, flashlamp-pumped Nd:YAG laser with a maximum pulse repetition frequency of 20 Hz) is triggered and fires a 50-mJ,  $\sim$ 7-ns, 1064-nm pulse to perform LIBS analysis on the particle. The LIBS emission is collected in the backward direction, imaged into a spectrometer (150 g/mm, 500-nm blaze grating), and detected with an intensified charge-coupled device. Since the emission lines of interest range from  $\sim$ 280 nm (Mg) to  $\sim$ 766 nm (K), collection and focusing of LIBS emission is accomplished with off-axis parabolic mirrors to eliminate chromatic aberration. Additionally, the integrated elastic scatter, fluorescence, and LIBS laser intensity are acquired and saved with each single-particle LIBS spectrum.



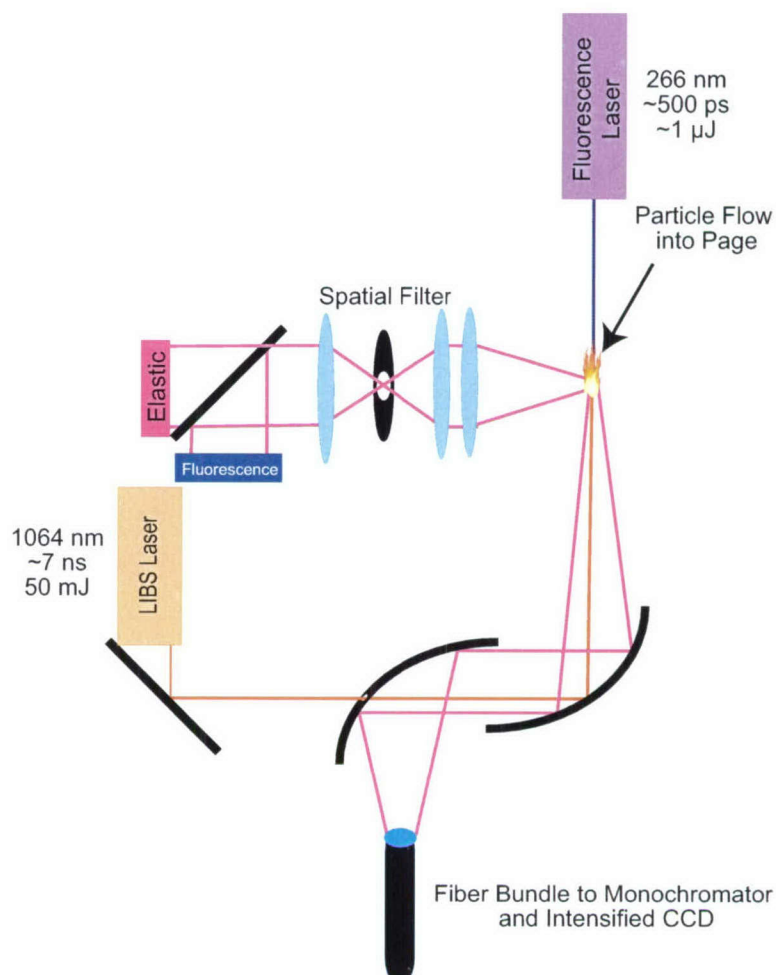


Figure 1-1. Conceptual schematic of fluorescence-cued laser-induced breakdown spectroscopy (LIBS) instrument.

Representative single-particle LIBS spectra of a variety of simulant organisms are shown in Figure 1-2. Each aerosol dissemination was mono-disperse with mean particle sizes of  $3 \mu\text{m} \pm 0.5 \mu\text{m}$ . Each organism has a readily detectable elemental signature. Bacterial spores (Bg) contain a significant amount of calcium, while the vegetative samples (*Pantoea agglomerans* and *Yersinia rhodei*), the toxin simulant (ovalbumin), and the viral simulant (MS2) contain mainly Na and K. Since preparation methods may change the elemental content of the organism, the effects of a variety of preparation and washing methods on the LIBS signatures were measured. The main effect of washing was to reduce, but not eliminate, the Na and K signals. Preparation methods (changes in growth media) did not appear to play a major role in

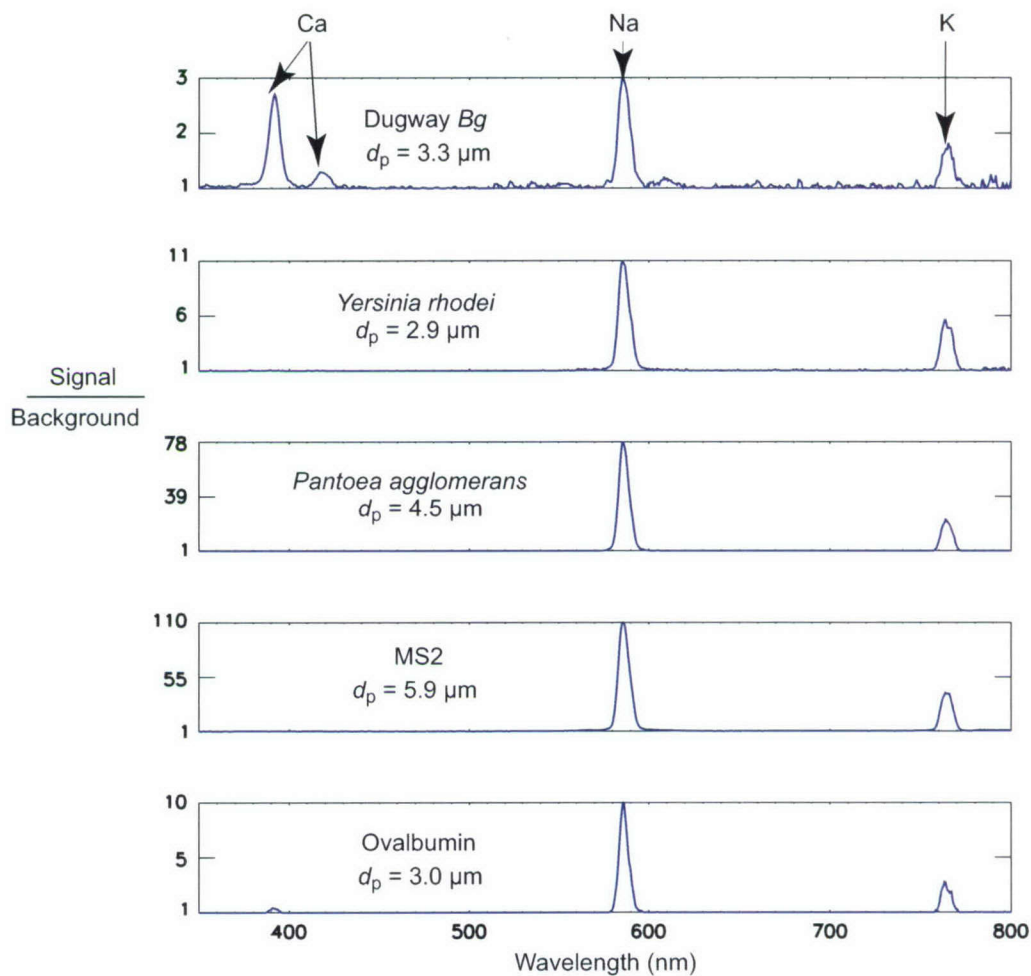


Figure 1-2. Representative single-particle spectra of five types of simulants. Included in each spectrum is the mean particle diameter  $d_p$  of the aerosol used for each measurement. All samples were washed once with deionized water to remove the saline buffer used in the production of lyophilized samples. Since LIBS measurements are limited by signal-to-background ratio, rather than absolute signal strength, the spectra are plotted in units of signal divided by background; therefore, areas of the spectrum with no signal from the particle have a ratio of 1.

determining the LIBS signature. LIBS signatures of Bg were also measured as a function of particle size in order to determine detection limits and to ensure that the signature does not change with particle size. Particles down to  $\sim 2\text{-}\mu\text{m}$  diameter produced acceptable signal-to-noise LIBS spectra, and changes in particle size influenced both the absolute magnitude of the signal and to a lesser extent the ratios among atomic lines.

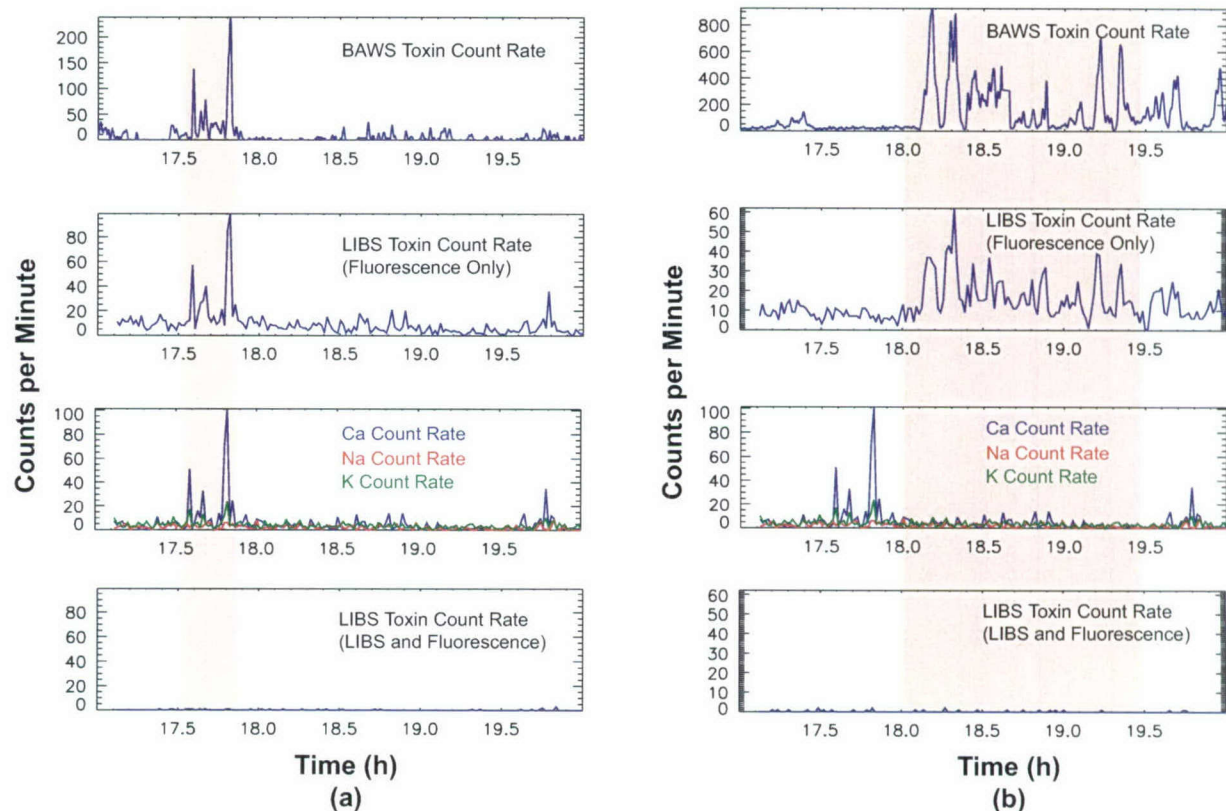


Figure 1-3. (a) Time series of concurrent Biological Agent Warning Sensor (BAWS) and LIBS measurements of outdoor aerosol. From top to bottom, plots show BAWS “toxin” counts as a function of time; LIBS sensor measurements of toxin-like particles (by fluorescence signature only); the number of particles containing Ca, Na, and K; and the number of particles that appear toxin-like when both the elemental information and fluorescence signatures are utilized. (b) Similar time series for Bg-like particles.

The LIBS test bed was taken outdoors to test its ability to discriminate bioaerosol simulants from real, ambient aerosol particles. The LIBS instrument was co-located with a Biological Agent Warning Sensor (BAWS) in the Lincoln Laboratory parking lot. By concurrently collecting data with the LIBS sensor and the BAWS, the LIBS data could be correlated to fluorescent-particle populations detected by the BAWS. Figure 1-3(a) displays a timeline of the “toxin” particle count rate from the BAWS along with the LIBS instrument’s total toxin-like fluorescent-particle count rate, element-specific count rate, and LIBS toxin count rate (includes elemental information). Clearly, the two sensors see the same three spikes of fluorescent, toxin-like particles with fluorescent detection. Additionally, nearly all of these particles contain both Ca and K. However, the LIBS signature for a toxin is the presence of detectable levels of Na and K. Therefore, since Na is absent in nearly all of the particles, the LIBS signature can be used to



discriminate against these particles, resulting in a near-zero count rate for particles that appear toxin-like when both the fluorescence and LIBS signatures are used. Figure 1-3(b) shows a similar instance for discrimination against Bg-like particles (for Bg, the simultaneous presence of Ca, Na, and K is required in addition to the appropriate fluorescence signature). Clearly, in these cases, the addition of LIBS adds significant value for discrimination.

Thus, LIBS has demonstrated substantial discrimination against outdoor aerosols when combined with fluorescence detection. It is important to note that many naturally occurring aerosol particles contain common elements such as Ca, Na, and K. Therefore, it is unlikely that LIBS alone can provide much discrimination. However, within the subset of fluorescence particles in the outdoors, LIBS can provide increased discrimination by detecting these elements.

J. D. Hybl  
S. M. Tysk  
M. Hiett

#### REFERENCES

1. G. Gould and A. Hurst, *The Bacterial Spore* (Academic, London, 1969).
2. J. Carranza, B. Fisher, G. Yoder, and D. Hahn, *Spectrochim. Acta, Part B* **56**, 851 (2001).

## 2. ELECTRO-OPTICAL MATERIALS AND DEVICES

### 2.1 NARROW-LINEWIDTH, HIGH-POWER 1556-nm SLAB-COUPLED OPTICAL WAVEGUIDE EXTERNAL-CAVITY LASER

Single-longitudinal-mode lasers having narrow linewidth are required for coherent laser radar and optical communications, photonic synthesis of low-noise microwave signals, and precision optical metrology. To date, solid state lasers have exhibited a smaller quantum-limited (Schawlow-Townes) linewidth than semiconductor lasers because of their relatively larger intracavity powers, smaller intracavity losses, and negligible free-carrier gain/index coupling. Semiconductor external-cavity lasers (ECLs) incorporating fiber Bragg gratings (FBGs) [1] have demonstrated linewidth  $<100$  kHz [2],[3] and high output power (27 mW at 1535 nm [4], 1.35 W at 780 nm [5]). Here, we report the first investigation of a narrow-linewidth ECL based on the slab-coupled optical waveguide (SCOW) gain medium [6]–[8]. The semiconductor SCOW architecture has a number of advantages for realizing high-power, low-noise lasers, including a large fundamental mode ( $>4 \times 4 \mu\text{m}$ ), low optical loss that allows long length for efficient heat removal, and low optical confinement. Previously, we reported a single-pass SCOW amplifier (SCOWA) with 13-dB fiber-to-fiber small-signal gain and 630-mW saturation output power [8]. We now describe both the development of a 1.5- $\mu\text{m}$  InGaAsP/InP curved-channel, double-pass SCOWA and the demonstration of an FBG ECL using this amplifier.

The curved-channel SCOWA material design (see inset of Figure 2-1) consists of a thick, lightly  $n$ -doped InGaAsP waveguide ( $h = 5 \mu\text{m}$ ,  $5 \times 10^{16} \text{ cm}^{-3}$  S,  $\lambda_G \sim 1.03 \mu\text{m}$ ) that is weakly coupled ( $\Gamma \sim 0.003$ ) to an InGaAsP multiple quantum-well active region. The design used here is similar to the one reported in [8], except four quantum wells are used instead of five and a  $p$ -doped InAlAs electron-blocking layer (150 nm,  $10^{17} \text{ cm}^{-3}$  Zn) is included between the multiple-quantum-well region and  $p$ -doped InP cladding layer. We note that the thickness and doping of this electron-blocking layer are not optimized. Single-lateral-mode operation was achieved by  $\text{CH}_4/\text{H}_2/\text{Ar}$  reactive-ion etching a ridge waveguide ( $w = 5.8 \mu\text{m}$ ) to an etch depth  $d$  of  $2.6 \mu\text{m}$  ( $t = 4.5 \mu\text{m}$ ). Other fabrication details can be found in [8].

A double-pass, single-ended SCOWA was realized by using a curved-channel waveguide geometry that provides both a high-reflectivity flat facet and a low-reflectivity angled facet (see Figure 2-1). Because of the very low transverse index contrast ( $\Delta n/n = 7 \times 10^{-4}$ ) of the SCOWA, a large radius of curvature ( $r = 10$  cm) was used to minimize the waveguide bend loss. The attained facet angle was  $5^\circ$ . The bend loss for this geometry was estimated to be  $<0.1$  dB. The angled input/output facet was antireflection (AR) coated and the flat rear facet was coated for high reflectivity ( $R > 95\%$ ). The total device length was 1 cm. The SCOWA was mounted junction-side up to a Cu-W heatsink and temperature controlled using a thermoelectric cooler.

Double-pass gain spectra of the curved-channel SCOWA were measured using a tunable laser, optical circulator, and power meter, as shown in Figure 2-1. A Flexcore 1060 fiber, cleaved at a  $6^\circ$  angle



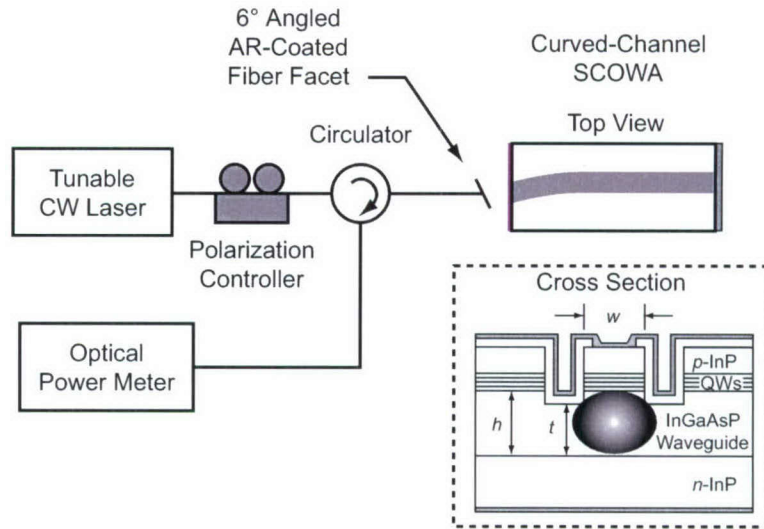


Figure 2-1. Equipment configuration for gain spectra measurements of curved-channel slab-coupled optical waveguide amplifier (SCOWA). Top view and cross section of the SCOWA device are also shown.

and AR coated, was directly coupled to the SCOWA angled facet at an angle that maximized the coupling efficiency. The measured gain spectra, shown in Figure 2-2, indicate a peak fiber-to-fiber gain of 22 dB for an input power of 0.65 mW at a bias current  $I$  of 4.0 A. Thus, the peak fiber-coupled output power observed was 103 mW. The 3-dB gain bandwidth is in excess of 100 nm. We did not attempt to measure the saturation output power of the double-pass SCOWA owing to the maximum power rating (200 mW) of the circulator. With no input signal, the fiber-coupled spontaneous emission power was 2.7 mW at a current of 4.0 A. The SCOWA-to-fiber coupling efficiency was measured to be  $\sim 50\%$ .

The ripples in the gain spectra of Figure 2-2 are due to residual facet reflectivity. Additional gain spectra measured using a smaller wavelength step of 2 pm (data not shown) revealed well-defined Fabry-Perot fringes with peak-to-valley ratios (PVRs) of 0.3, 0.5, 0.7, and 0.6 dB for bias currents of 1, 2, 3, and 4 A, respectively. The Fabry-Perot fringe period of the 1-cm-long cavity was measured to be  $\Delta\lambda = 33$  pm ( $\Delta\nu = 4.1$  GHz). By combining the Fabry-Perot PVR data with the gain data and the estimated 50% coupling efficiency, the residual reflectivity of the angled AR-coated facet was estimated to be  $R < 3 \times 10^{-6}$ .

The SCOW external-cavity laser (SCOWECL) was constructed by butt coupling the SCOWA to a FBG, as shown in Figure 2-3, using a laser-welded fiber-pigtailing assembly process. The FBG, fabricated in Flexcore 1060 fiber, had a peak reflectivity of 50% and a full width at half-maximum (FWHM) bandwidth of 50 pm (6.2 GHz) that was centered at 1556.1 nm. The FBG was cleaved at an  $11^\circ$  angle to allow maximum coupling when the SCOWA and FBG facets are parallel. The FBG was attached to an aluminum plate and was not temperature stabilized.

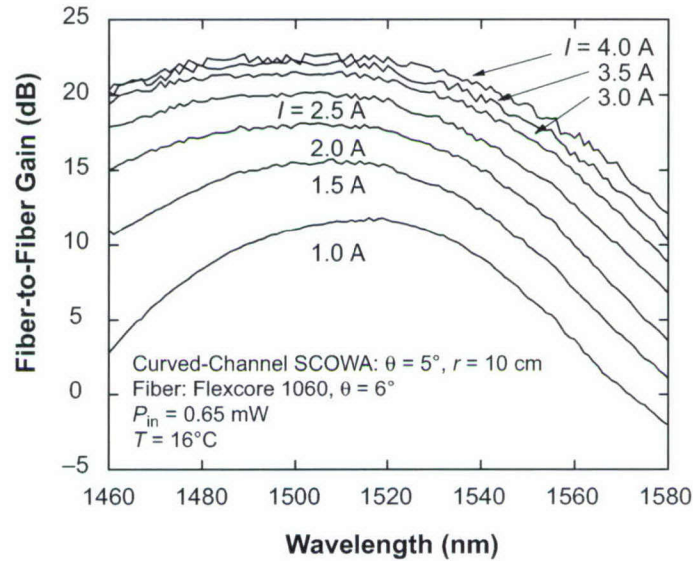


Figure 2-2. Measured double-pass fiber-coupled gain spectra of curved-channel SCOWA. Tunable-laser wavelength step  $\Delta\lambda = 1$  nm.

The SCOWECL was characterized using the configuration depicted in Figure 2-3. The threshold current of the laser-welded SCOWECL was 2 A, which was significantly larger than the threshold current ( $\sim 1$  A) obtained during manually coupled bench testing. This difference in threshold current is attributed to coupling misalignment in the laser-welded assembly. A scanning Fabry-Perot interferometer having a 2-GHz free-spectral range (FSR) and a 10-MHz resolution was used to determine if the laser was operating with a single or with multiple longitudinal modes. The laser operated with multiple longitudinal modes over much of the current range investigated ( $I = 2$ –4 A). Stable single-mode operation was achieved only for several small current ranges ( $\Delta I \sim 20$  mA) spaced between 2.5 and 3.5 A.

The rf spectrum of the SCOWECL optical output power was measured using a wideband (40 GHz) photodiode, a microwave amplifier (gain 29 dB, bandwidth 20 GHz), and a microwave spectrum analyzer. Residual longitudinal mode beats were observed at a frequency spacing of 1.3 GHz. This mode frequency spacing, in conjunction with the 4.1-GHz SCOWA mode spacing discussed above, reveals that the effective length of the FBG external cavity is 5.4 cm. We note that approximately five of the SCOWECL longitudinal modes are present within the 3-dB bandwidth of the FBG. The presence of multiple modes within the FBG passband may be the reason why single-mode operation was attained only for narrow current regions as described above. In future designs, we intend to reduce the external-cavity length to improve single-mode operation.



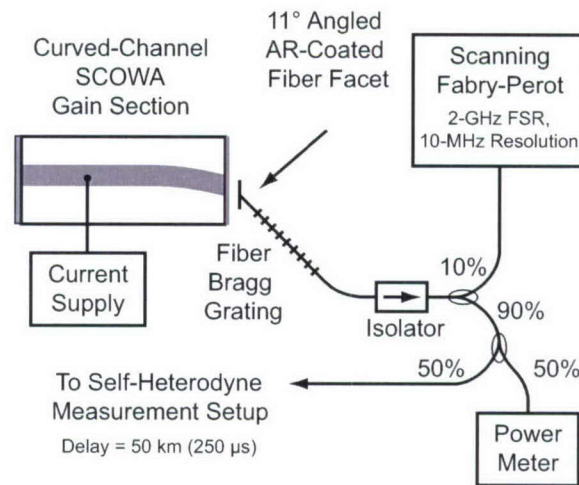


Figure 2-3. SCOW external-cavity laser (SCOWECL) comprising a curved-channel SCOWA gain section, fiber Bragg grating, and output isolator. The laser characterization setup is also shown.

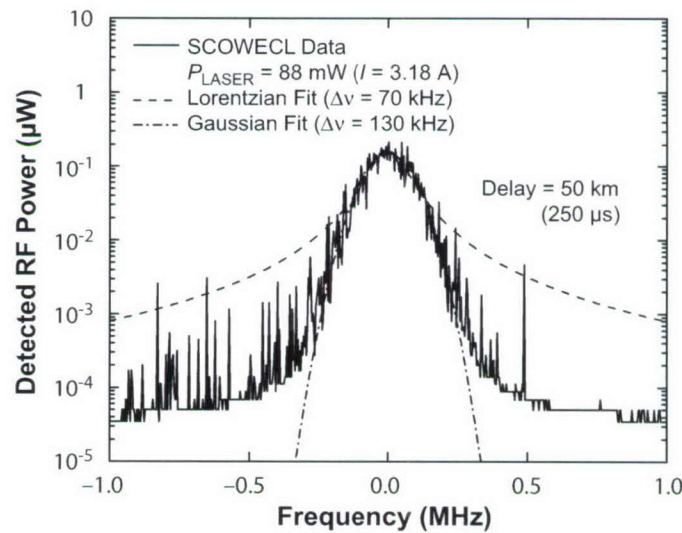


Figure 2-4. Self-heterodyne linewidth measurement of SCOWECL operating with 88-mW output power. Both Lorentzian (dash) and Gaussian (dash-dot) fits are shown.

The SCOWECL linewidth was estimated using the self-heterodyne measurement technique [9]. The differential delay in the Mach-Zehnder was 250  $\mu$ s, corresponding to 50 km of SMF-28 fiber. The acousto-optic frequency shift was 35 MHz. The resulting self-heterodyne power spectrum corresponding to a laser output power of 88 mW ( $I = 3.18$  A) is shown in Figure 2-4. The self-heterodyne spectrum is well fit by a Gaussian lineshape over two orders of magnitude. We note that the self-heterodyne spectrum is the autoconvolution of the actual laser noise spectrum. Thus, for a Gaussian lineshape, the width of the self-heterodyne spectrum FWHM is  $\sqrt{2}$  larger than the laser spectrum FWHM. The laser spectrum FWHM linewidth extracted from the Gaussian fit data is 130 kHz. The Gaussian lineshape indicates that the laser is technical-noise limited (e.g., current-supply noise) and not quantum-noise limited. A laser that is quantum-noise limited will have a Lorentzian lineshape. The SCOWECL lineshape is clearly not Lorentzian as is evident in the fit data in Figure 2-4 (dashed line).

Thus, we have developed a 1.5- $\mu$ m high-power ( $P > 100$  mW), double-pass, curved-channel semiconductor optical amplifier based on the SCOW concept. This large-transverse-mode optical amplifier was butt coupled to a narrow-bandwidth (50 pm) FBG to realize an external-cavity laser that demonstrated a linewidth of 130 kHz at an output power of 88 mW and an operating wavelength of 1556 nm. The linewidth data are well fit by a Gaussian lineshape, indicating that the linewidth is technical-noise and not quantum-noise limited. It is expected that the linewidth can be greatly reduced by reducing the noise of the current supply. The high power, low optical loss, and large mode-volume characteristics of the semiconductor SCOW gain medium are expected to enable narrow-linewidth lasers having performance approaching that of lasers based on solid state gain media.

P. W. Juodawlkis	J. J. Plant
F. J. O'Donnell	L. J. Missaggia
R. K. Huang	J. P. Donnelly

## REFERENCES

1. C. A. Park, C. J. Rowe, J. Buus, D. C. J. Reid, A. Carter, and I. Bennion, *Electron. Lett.* **22**, 1132 (1986).
2. D. M. Bird, J. R. Armitage, R. Kashyap, R. M. A. Fatah, and K. H. Cameron, *Electron. Lett.* **27**, 1115 (1991).
3. Z. Sheng, W. Cailing, and Q. Qinian, *Proceedings of the Conference on Lasers and Electro-Optics* (Optical Society of America, Washington, DC, 1999), p. 918.
4. P. A. Morton, V. Mizrahi, T. Tanbun-Ek, et al., *Appl. Phys. Lett.* **64**, 2634 (1994).

5. A. K. Goyal, P. Gavrilovic, and H. Po, *Appl. Phys. Lett.* **73**, 575 (1998).
6. J. N. Walpole, J. P. Donnelly, P. J. Taylor, et al., *IEEE Photon. Technol. Lett.* **14**, 756 (2002).
7. J. P. Donnelly, R. K. Huang, J. N. Walpole, L. J. Missaggia, C. T. Harris, J. J. Plant, R. J. Bailey, D. E. Mull, W. D. Goodhue, and G. W. Turner, *IEEE J. Quantum Electron.* **39**, 289 (2003).
8. P. W. Juodawlkis, J. J. Plant, R. K. Huang, L. J. Missaggia, and J. P. Donnelly, *Proceedings of the Lasers and Electro-Optics Society Annual Meeting* (IEEE, Piscataway, NJ, 2003), p. 425.
9. T. Okoshi, K. Kikuchi, and A. Nakayama, *Electron. Lett.* **16**, 630 (1980).



### 3. SUBMICROMETER TECHNOLOGY

#### 3.1 A VARIABLE-TRANSMITTANCE APODIZING FILTER AT 157 nm

Apodizing techniques have been developed in a number of optical imaging and processing systems to optimize the balance of power between the primary lobe and sidelobes of a propagating wavefront. A Gaussian transmission function has proven to be both common and versatile [1]–[3], but the fabrication of these filters typically requires a complex thin film deposition process. Here, we report on the design, assembly, and use of a Gaussian apodizer, which is achieved by filling the gap between two optical surfaces with a suitably absorbing gas. This apodizer has certain unique desirable properties. The degree of apodization is dynamically variable over a wide range, on the scale of minutes, controlled by varying the pressure and flow rate of the gas. Such capability can have many applications. For instance, in photolithography a variable apodizer could be dynamically tuned to optimize depth of focus, central lobe width, and contrast for certain geometries or when switching between different photomasks or different illumination modes. Furthermore, the concept is applicable to wavelengths from the vacuum-uv to the infrared, with essentially the same setup. In addition, it is especially useful when used with high-power lasers, which can damage more conventional thin film or solid apodizers.

Our demonstration has been carried out at 157 nm, where we constructed an instrument to measure the low-angle scatter of optical surfaces, such as the scatter that can lead to flare in optical lithographic systems. The choice of absorber gas is determined primarily by the wavelength. At 157 nm oxygen is suitable since it is absorptive below  $\sim 185$  nm. The Gaussian apodization is obtained by flowing oxygen at controlled partial pressures between the opposing spherical surfaces of two custom meniscus lenses. Under the paraxial approximation the optical path difference between the elements scales quadratically with the radial distance  $r$  from the optical axis. Filling the space between the mated lens faces with an absorptive medium with absorption coefficient  $k_{\text{gas}}$  results in a Gaussian transmission factor for the apodizing filter  $P(r)$ :

$$P(r) = e^{-\frac{2}{R}k_{\text{gas}}r^2} \quad (3.1)$$

where  $R$  is the radius of curvature of the mated lens faces. At 157 nm,  $k_{\text{gas}}$  of molecular oxygen is  $150 \text{ cm}^{-1}$  at one atmosphere [4].

The optical system that includes the apodizer is shown in Figure 3-1. It uses a pulsed 157-nm fluorine excimer laser (Lambda Physik LPF 220) operating at 200 Hz. Since apodization is most efficient with a spatially coherent source, the multimode output of the laser was first spatially filtered with the aid of two pinholes fabricated in 25- $\mu\text{m}$ -thick tungsten membranes. The apodizer comprises two spherical meniscus lenses, fabricated in fluorine-doped fused silica, each having surface radii of curvature of 31.25 and 29.04 mm. The 157-nm focal length of each meniscus is 200 mm. The meniscus lenses are mounted in a vapor cell allowing oxygen gas to flow between them. To distribute oxygen uniformly through the cell,



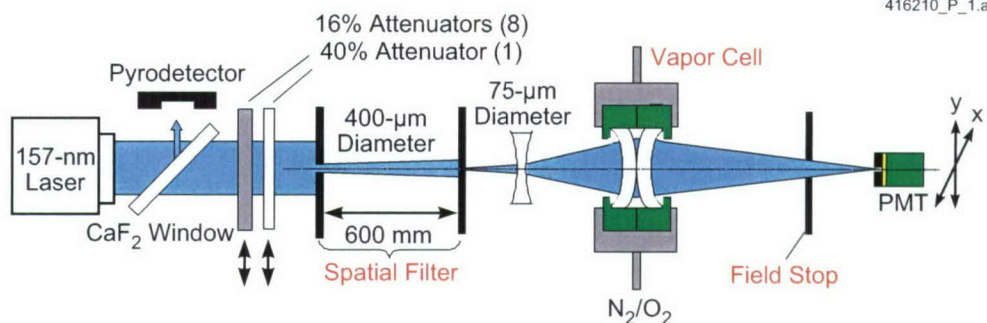


Figure 3-1. Schematic drawing of experimental test bed for apodizer.

three separate inlets and outlets are used. All optical elements are contained in aluminum enclosures interconnected with aluminum tubes and purged with boil-off nitrogen, so as to eliminate the chance of photoinduced contamination.

Although the use of an absorptive gas allows a simple delivery system to be constructed, the gas phase dynamics under laser radiation must be considered when determining the appropriate flow rate. In the present situation, oxygen readily dissociates under irradiation and forms ozone (O<sub>3</sub>), which at 157 nm is approximately three times more transparent [4], and atomic oxygen in its ground state, O<sup>3</sup>P, which is transparent at 157 nm. Thus, in general the value of  $k_{\text{gas}}$  in Equation (3.1) will depend on the steady-state concentrations of all three species of oxygen. These concentrations in turn will depend on the various chemical and photochemical rates and on the residence time of the gas. The temporal evolution of molecular oxygen, ozone, and atomic oxygen is predicted using the Chapman reaction model, which was developed to simulate the behavior of ozone in the upper atmosphere [5]. For the average intensities of our low-angle scatterometer ( $<1 \text{ mW/cm}^2$ ), we find that ozone forms on time scales longer than minutes. With the volume between the meniscus lenses being under  $1 \text{ cm}^3$ , and the flow rates  $\sim 1 \text{ liter/min}$ , the residence time is  $<100 \text{ ms}$ . This is at least several orders of magnitude smaller than the time scale of ozone formation, and therefore the ozone concentration (and the atomic oxygen concentration) under our experimental conditions is negligible.

The efficiency of the apodizer is measured experimentally by spatial mapping of the intensity profile of the beam, both at its center and in the wings, where the diffracted signal is orders of magnitude lower than in the primary lobe. This task is carried out with a profiler, seen in Figure 3-1, based on a photomultiplier tube (PMT) (Perkin Elmer channel model 911), which incorporates a CsI photocathode that is solar blind above 230 nm. The detector is mounted on a precision x-y stage, allowing two-dimensional profiles to be performed. The photomultiplier linearity is determined by comparing its output with that of a pyrodetector standard. In performing measurements over the seven orders of magnitude required by our application, a set of attenuators are cycled into the beam line. These attenuators

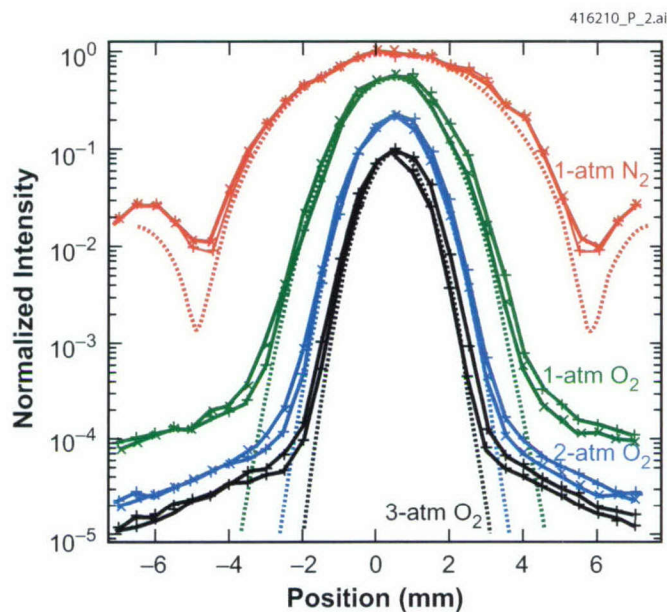


Figure 3-2. Intensity map through flood-exposed apodizer cell at different levels of oxygen. Each solid trace represents a separate  $x$  or  $y$  directional scan. The dashed curves represent the theoretical intensity maps. In order to match the position of the diffraction nulls, the Airy distribution for a  $65\text{-}\mu\text{m}$ , rather than  $75\text{-}\mu\text{m}$ , pinhole has been used in computing the theoretical curves.

are fabricated by depositing a thin film of platinum on  $\text{CaF}_2$ . They have transmission of 16% or 40%, depending on the thickness of the film, and are calibrated individually in situ using a pyrodetector. The appropriate combination of attenuators is chosen, in order to maintain a suitable signal level on the photomultiplier. A portion of the input beam is also split off by a  $\text{CaF}_2$  window preceding the attenuators and is detected by a pyrodetector for reference measurements.

To test the operation of the apodizing cell, intensity measurements were first performed directly after the apodizing cell. The cell is flood illuminated by locating the diverging lens at the back focal plane of the lens combination in the apodizer cell. The intensity pattern of the resulting collimated beam is mapped by placing the scanner 100 mm from the meniscus lenses. The pattern is shown in Figure 3-2 for three concentrations of  $\text{O}_2$  and for the control case of an unapodized beam, when transparent  $\text{N}_2$  flows through the cell. The dotted lines are theoretical curves, based on multiplying the Airy disk distribution emanating from the  $75\text{-}\mu\text{m}$  pinhole by the Gaussian transmission factor given in Equation (3.1). The introduction of oxygen clearly shows a marked sharpening of the central lobe and complete elimination of the sidelobes. The experimental intensity profiles agree very well with the predicted values at the three different oxygen levels when  $k_{\text{gas}}$  is that of oxygen rather than of ozone, in agreement with the chemical kinetics analysis above. The higher intensity levels in the tails with apodization are attributed primarily to multiple



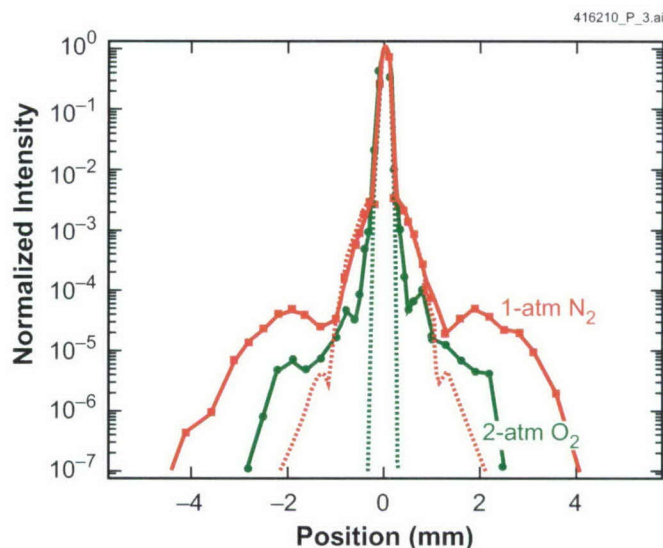


Figure 3-3. Intensity map in image plane with 1-atm  $N_2$  and 2-atm  $O_2$  flowing through the apodizing cell. The dashed curves represent the theoretical profiles.

reflections off the uncoated optics. Ray tracing simulations indicate these beams come to a focus approximately halfway between the detector and lens combination before rapidly diverging, thus manifesting themselves as diffuse scattering. An additional feature of the data shown in Figure 3-2 is a reduction in the peak intensity. This is due to a small gap between the meniscus lenses, which was maintained to prevent contact damage during sealing the back sides of the lenses.

Similar profiling measurements are performed in the image plane after repositioning the divergent lens to produce a 1:1 coherent imaging system, so that the 75- $\mu\text{m}$  pinhole produces a geometric image of 75  $\mu\text{m}$  in the absence of aberrations. This is the configuration for using the apodizer as part of a low-angle scatterometer. In this arrangement a 4-mm-diameter field stop is placed right before the sample being measured in order to limit the degree of scattered light from the lens entering the detector plane. Figure 3-3 shows the experimental results compared with the predicted curves. For clarity, only one line scan (x direction) is shown, and the traces have been normalized to unity peak levels. The simulated results incorporate the primary through fourth-order spherical aberrations caused by the two spherical meniscus lenses. Because of the high curvature of the optics, the effect of the spherical aberration is pronounced and can be clearly seen in the unapodized case by the broadened first sidelobe. With apodization the aberration is suppressed, as a smaller effective portion of the lens is used. Figure 3-3 also shows an approximately 10 $\times$  reduction in the relative magnitude of the diffraction-induced first sidelobe, at approximately  $\pm 2$  mm, as a clear result of apodization.

Another effect noticeable in Figure 3-3 is a discrepancy between the experimentally achieved intensity profile and the simulated curves, which becomes significant at normalized intensity levels of  $\sim 10^{-4}$  and below. This effect is probably caused by higher-order aberrations and by scattering that passes through the field stop.

T. M. Bloomstein  
D. E. Hardy

### 3.2 FIELD EMISSION AT $10 \text{ V cm}^{-1}$ WITH SURFACE EMISSION CATHODES ON NEGATIVE ELECTRON AFFINITY INSULATORS

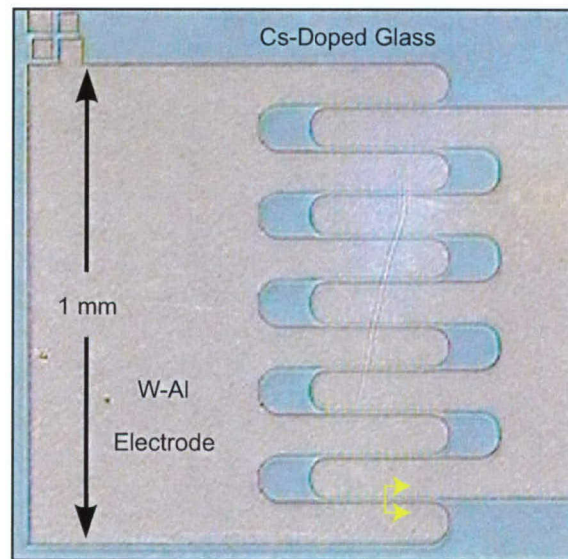
Surface emission cathodes, first reported by Dittmer [6] in 1972, consisted of two electrodes placed on an insulating substrate. A thin discontinuous metal film, usually  $\sim 10 \text{ nm}$  of Au, is deposited between the electrodes. When sufficient bias voltage was placed across these electrodes, electrons were emitted into vacuum. The ratio of the emitted current to the current flowing between the electrodes, the cathode efficiency, was  $1 \times 10^{-4}$  to  $1 \times 10^{-2}$  [6]–[9]. By replacing the Pyrex glass used by Dittmer with a negative electron affinity (NEA) insulator, improving the electrode geometry, and removing the discontinuous metal film, we have obtained efficiencies  $> 1 \times 10^3$ .

The fabrication process begins with the formation of a cesium-doped glass that serves as the NEA emission surface. The  $\text{Cs}_2\text{Si}_4\text{O}_9$  glass layer is formed by spinning a water-based mixture of 20-nm-diameter  $\text{SiO}_2$  colloids [10] and CsOH on Si wafers previously coated with 100 nm to 1  $\mu\text{m}$  of thermal  $\text{SiO}_2$ . The resulting film is prebaked to  $200^\circ\text{C}$  and transferred without cooling to an oven ramped to  $800^\circ\text{C}$  and then allowed to cool to room temperature. The resulting film of  $\text{Cs}_2\text{Si}_4\text{O}_9$  is  $\sim 0.8 \mu\text{m}$  thick. The interdigitated electrodes, seen in Figure 3-4(a), are formed from 70 nm of electron-beam-evaporated Al and 150–300 nm of W. The W film is patterned using standard lithography and reactive ion etching (RIE) in  $\text{CF}_4$ . The W film is then undercut by etching the Al in a commercial phosphoric base solution, as seen in Figure 3-4(b). The photoresist used to pattern the W film is removed using  $\text{O}_2$  RIE to avoid contamination from organic solvents, and the sample is stored in dry nitrogen. Just before testing, the cathodes are subjected to an  $\text{O}_2$  plasma and rinsed in deionized water. Electrical contact to the back of the silicon substrate is made either with silver paint or electron beam evaporated Ti.

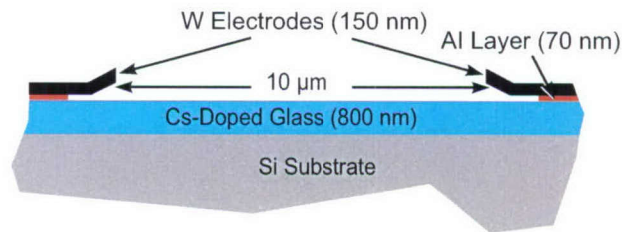
Testing was performed in an oil-free cryopumped vacuum system at a pressure consisting primarily of  $1 \times 10^{-6}$  to  $1 \times 10^{-7}$  Pa of water vapor. Before testing, the cathode is baked to  $\sim 200^\circ\text{C}$  for  $> 12 \text{ h}$ . After emission, cathodes can be exposed to dry air without damage.

Emission occurs when electrons tunnel from the metal electrode onto the insulator surface and from there are thermally or ballistically emitted into vacuum. The tunneling of electrons from the metal to the insulator surface is facilitated by a submicron gap between the electrode and the insulator surface, shown in Figure 3-4(b). In this gap the barrier for electrons to tunnel from the metal electrode onto the insulator is





(a)



(b)

Figure 3-4. Surface emission glass cathode: (a) Optical micrograph of two metal electrodes on a glass-silicon substrate, and (b) schematic cross section of the cathode for the region marked with yellow arrows in (a). The electrodes seen on the left and right sides of (b) are fabricated with a tungsten/aluminum structure that is undercut to form a submicrometer gap between the tungsten layer and the glass surface.

greatly decreased by image charges in both the metal and the insulator. Cathodes without this undercut have either no emission or emission reduced by several orders of magnitude. Once on the insulator the electrons are bound by  $\sim 0.4$  eV through their image charge [11],[12]. This low binding energy allows electrons to evaporate into vacuum.

During testing, the silicon substrate and one of the electrodes are grounded as shown in Figure 3-5, and the bias on the remaining electrode is adjusted as described below. The electrical properties of one of

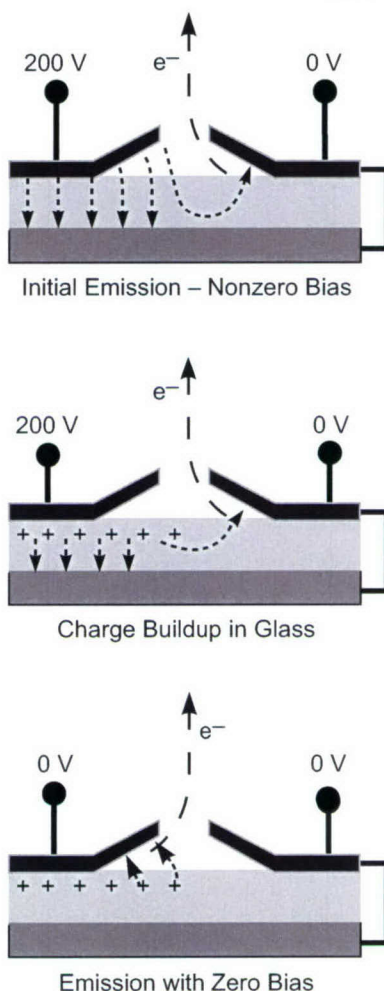


Figure 3-5. Schematic cross section of cathode indicating the distribution of charge and electric field as one electrode is biased to 200 V and then grounded, with the other electrode and the silicon substrate both grounded. Diagrams illustrate cathode (a) under initial testing, (b) after several minutes to several hours of operation, and (c) after bias voltage is removed.

the better glass cathodes during initial testing are shown in Figure 3-6(a). The bias voltage is increased from 0 to 230 V. At 110 V, measurable emission current,  $>5 \times 10^{-12}$  A, occurs and quickly increases to  $1 \times 10^{-6}$  A. The bias voltage is then decreased from 210 to 0 V. Although the electrode is still positively biased, its current becomes negative and equal in amplitude to the anode current. As the device is operated, positive traps form under the most positive electrode, shown in Figure 3-5(b), and these traps supply

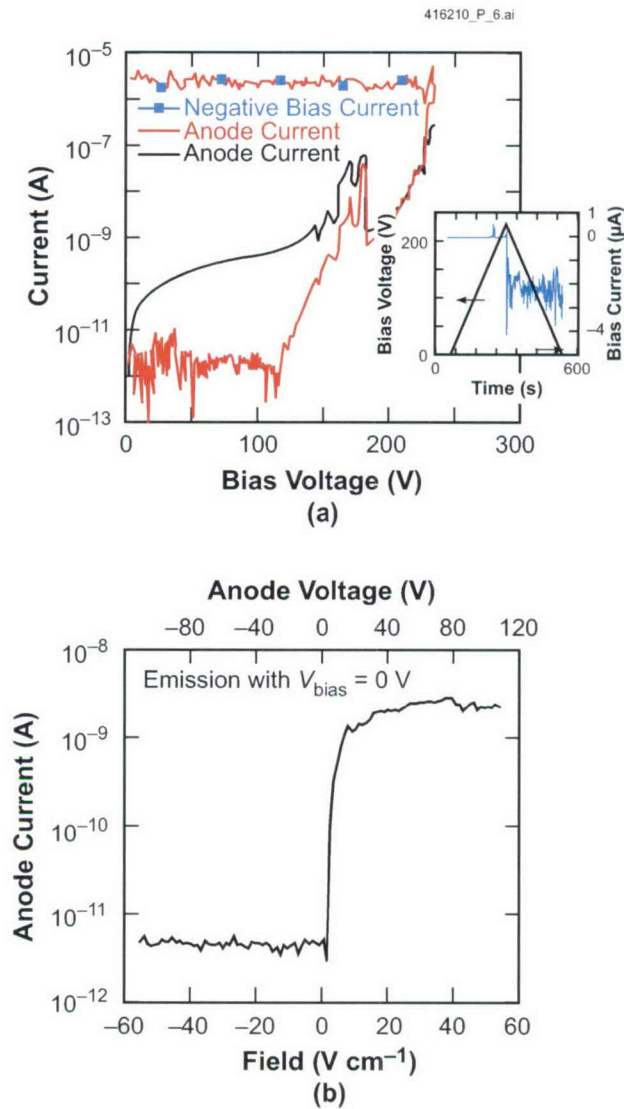


Figure 3-6. (a) Electrical properties of one of the better cathodes during its first testing, with the inset showing bias voltage and bias current as a function of time. The bias current remains negative after the bias voltage was decreased. (b) Anode current as a function of anode voltage and surface electric field into vacuum. After emission is initiated with a bias voltage of  $\sim 200$  V, the bias voltage is held at 0 V and the anode voltage is swept from 200 to  $-200$  V.

sufficient electric field to pull electrons out of the metal onto the insulator surface. Once the emission is initiated and the traps are formed, the emission can continue for several hours without bias, as seen in Figure 3-5(c).

A crude measurement of the emitted electron energies was obtained by varying the anode voltage, as shown in Figure 3-6(b). For an anode consisting of a 1-mm-diameter wire, 1 cm above and parallel to the cathode surface, a measurable emission current is obtained for anode voltages as low as 20 V, which represents an average surface electric field into vacuum at the cathode of  $<10 \text{ V cm}^{-1}$ . During emission with the anode at 1000 V, the exposed glass substrate charges up to several hundred volts. We speculate that this is the result of positive ions from the anode, which may be important for the continued 0-V bias emission.

These cathodes do not use geometry to enhance the electric field at atomically sharp tips, and because of this, catastrophic arcing and melting are uncommon. Instead, the cathodes fail slowly over a few seconds when over-voltaged. Since the cathode operation is not limited by the local high field concentrations, as with Spindt cathodes [13],[14], the emission current was experimentally found to scale with cathode area from  $1.3 \times 10^{-4}$  to  $1.5 \times 10^{-3} \text{ cm}^2$ .

M. W. Geis	D. L. Cooke*
S. Deneault	K. E. Krohn
M. Marchant	

## REFERENCES

1. D. W. Wilson, P. D. Maker, J. T. Trauger, and T. B. Hull, *Proc. SPIE* **4860**, 361 (2003).
2. A. F. Kurtz and M. E. Harrigan, *Proc. SPIE* **4095**, 176 (2000).
3. S. J. Wein and W. L. Wolfe, *Proc. SPIE* **967**, 27 (1988); *Opt. Eng.* **28**, 273 (1989).
4. H. Okabe, *Photochemistry of Small Molecules* (Wiley, New York, 1978), Chaps. 5–6.
5. P. Warneck, *Chemistry of the Natural Atmosphere* (Academic, New York, 1988), p. 100.
6. G. Dittmer, *Thin Solid Films* **9**, 317 (1972).
7. M. W. Geis, *Nature* **393**, 431 (1998).

---

\*Author not at Lincoln Laboratory.



8. P. G. Boziak, Y. A. Kulyupin, S. A. Nepijko, and V. G. Shamonya, *Thin Solid Films* **76**, 359 (1981).
9. H. Araki and T. Hanawa, *Thin Solid Films* **158**, 207 (1988).
10. Ammonia stabilized  $\text{SiO}_2$ -water colloid, Ludox AS made by Grave Davison.
11. C. C. Grimes and T. R. Brown, *Phys. Rev. Lett.* **32**, 280 (1974).
12. R. M. Osgood and X. Wang, *Solid State Phys.* **51**, 2 (1998).
13. P. R. Schwoebel, C. A. Spindt, and C.E. Holland, *Technical Digest of the 17th International Vacuum Nanoelectronics Conference* (IEEE, Piscataway, NJ, 2004), p. 232.
14. C. A. Spindt, I. Brodie, L. Humphrey, and E. R. Westerberg, *J. Appl. Phys.* **476**, 5248 (1976).

## 4. BIOSENSOR AND MOLECULAR TECHNOLOGIES

### 4.1 TESTING OF THE AFFINITY MAGNET CARTRIDGE

A compact, fieldable, easy-to-use self-contained cartridge has been developed, which produces polymerase chain reaction (PCR)-ready eluate from both liquid and solid sample types [1]. The baseline laboratory procedure for this device is the Affinity Magnet (AM) protocol, which uses magnetic beads to concentrate target from raw environmental or clinical sample [2]. Here, we report on tests of the two-valve commercial off-the-shelf (COTS) version of the cartridge. The tests used two targets, Ba spores and Ba vegetative cells, and two sample matrices, dirty environmental water and acid-washed sand.

The spores were produced at Lincoln Laboratory using standard protocols. Nutrient-deficient medium was spiked with overnight culture of either Ba or Btk and allowed to incubate at 37°C for 48 h. The cultures were washed a minimum of five times to remove extraneous DNA, incubated at 60°C for 60 min to ensure that no vegetative cells survived, and then washed again. Spore suspensions were quantified by counting colonies on plates streaked with sample and stored at 4°C. All tests were conducted using various quantities of Dynal M-270 2.7- $\mu$ m amine-functionalized magnetic beads, an elution buffer consisting of 500  $\mu$ L of a solution of 100  $\mu$ g of calf thymus DNA per mL of 0.01M sodium hydroxide, and various sizes of collection magnet in the processing chamber.

The liquid samples consisted of various concentrations of Ba spores or vegetative cells diluted in dirty environmental water. The soil samples consisted of 0.5–1 g of acid-washed sand, preseeded with Ba spores or vegetative cells and allowed to dry. During testing, each sand sample was formed into a slurry by mixing with 5 mL of distilled water in the sample input chamber. The effectiveness of the cartridge in concentrating the target present in a raw sample was determined by TaqMan PCR in an ABI 7700 system.

The results are presented in Figures 4-1 through 4-4, in which the PCR amplification plots are color coded. The brown or red curves indicate concentration controls of the target only, in clean water. The purple curves indicate concentration controls of the target only, in dirty environmental water; these are available only for liquid-sample test results. The green curves indicate the level of target in the eluate and are expected to be shifted to the left of the corresponding concentration control curves, signaling higher target levels in the sample after concentration. Finally, the blue curves indicate the level of unconcentrated target left behind in the supernatant and are expected to be shifted to the right of the corresponding concentration control curves, or not appear at all.

To determine the limit of detection (LOD) for Ba spores in dirty water, dilutions of spores were seeded into the water at concentrations from 0 to  $10^3$  spores/mL. Each cartridge was loaded with 5 mL of a dilution and then processed using 25 mg of magnetic beads for target capture. The collection magnet consisted of a chain of 10 magnetic spheres of 3/16-in. diameter. Target capture time was 5 min, bead capture time was 1 min, and elution time was 1 min. The detection limit from this experiment is

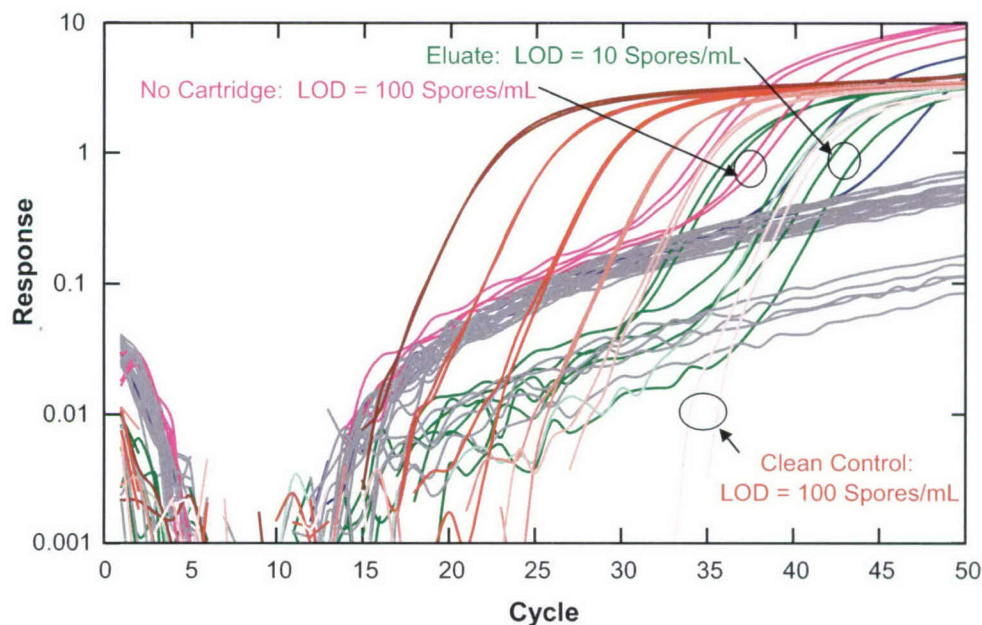


Figure 4-1. Detection of *Ba* spores seeded into dirty water using the Affinity Magnet (AM) cartridge protocol with a sample volume of 5 mL, a magnetic bead mass of 25 mg, a 10-sphere chain of collection magnets in the processing chamber, and a magnetic bead collection time of 1 min. Detection from eluate is observed down to 10 spores/mL compared to 100 spores/mL with no concentration. Note that eluate curves show reduced spurious background fluorescence that is commonly present in this type of sample, indicating that the AM concentration step has also eliminated most of the polymerase chain reaction (PCR) interferents. Also shown is the level of unconcentrated target left behind in the supernatant (blue curves).

10 spores/mL, as shown in Figure 4-1. This is an improvement of one order of magnitude over controls that were directly subjected to PCR without cartridge processing. Note that exposure of the collection magnet chain to the elution buffer was incomplete because of the small volume of the buffer compared to the size of the magnets. Recovery can be improved by modifying the procedure to allow complete immersion of the collection magnets in the buffer; this may be accomplished by reducing the size of the collection magnet and performing the target elution in the eluate vial instead of the middle processing chamber.

To determine the detection limit for *Ba* spores in sand, dilutions of spores were seeded into acid-washed sand at concentrations from 0 to  $10^6$  spores/mL of sand. Each cartridge was loaded with 1 g of seeded sand wetted with 5 mL of distilled water and processed using 15 mg of magnetic beads for target capture. The collection magnet consisted of two radially magnetic cylinders placed end to end. Target capture time was 5 min, bead capture time was 1 min, and elution time was 1 min. Elution was done by



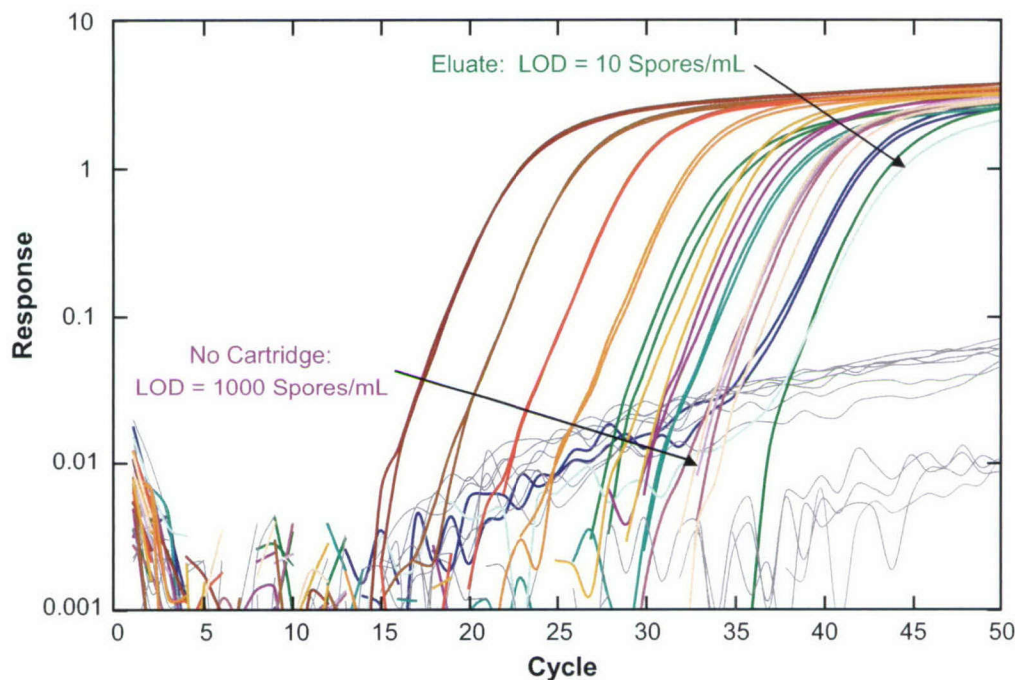


Figure 4-2. Detection of *Ba* spores seeded into sand using the AM cartridge protocol with a sample volume of 1 g of sand with 5 mL of distilled water, a magnetic bead mass of 15 mg, a two-cylinder-stack collection magnet in the processing chamber, and a magnetic bead collection time of 1 min. Detection from eluate is observed down to 100 spores/mL, compared to 1000 spores/mL with no concentration.

allowing the collection magnet to fall into the elution vial such that it was fully immersed in the elution buffer. Once the target was eluted from the magnetic beads, the collection magnet was transferred back into the lower valve of the assembly. The detection limit from this experiment is 100 spores/mL of sand, as shown in Figure 4-2. This is an improvement of one order of magnitude over samples that were directly subjected to PCR without cartridge processing.

Tests to determine the detection limits for *Ba* vegetative cells in dirty water and sand were done in which each cartridge was loaded with either 5 mL of dirty water seeded with *Ba* vegetative cells, or 1 g of seeded sand wetted with 5 mL of distilled water, and then processed. For target capture 15 mg of magnetic beads were used, and the collection magnet again consisted of two radially magnetic cylinders placed end to end. Target capture time was 5 min, bead capture time was 1 min, and elution time was 1 min. Elution was done by allowing the collection magnet to fall into the elution vial, such that it was fully immersed in the elution buffer. Once the target was eluted from the magnetic beads, the collection magnet was transferred back into the lower valve.

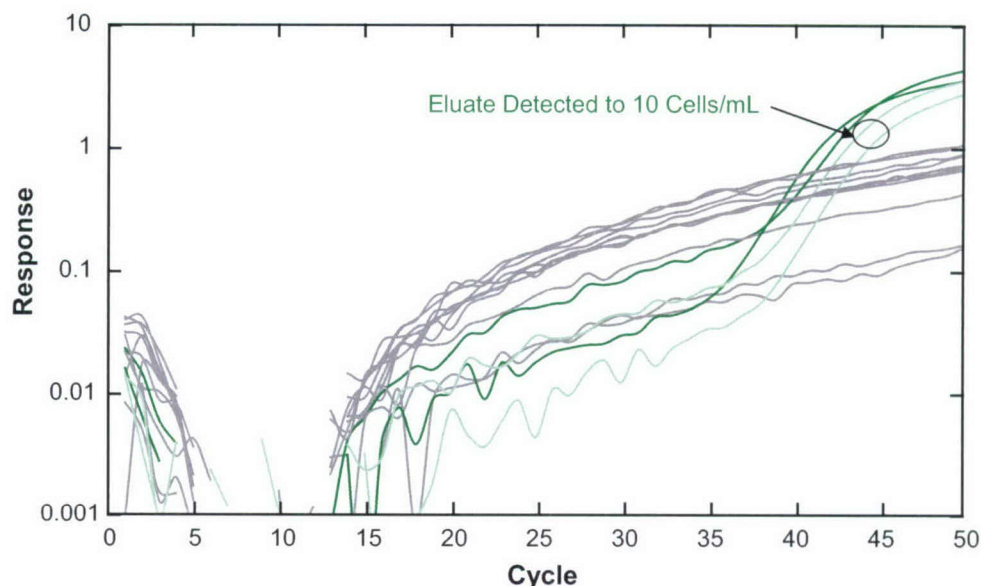


Figure 4-3. Detection of *Ba* vegetative cells seeded into dirty water using the AM cartridge protocol with a sample volume of 5 mL of liquid, a magnetic bead mass of 15 mg, a two-cylinder-stack collection magnet in the processing chamber, and a magnetic bead collection time of 1 min. Detection from eluate is observed down to 10 cells/mL, compared to no detection at all with unprocessed samples.

The LOD from dirty water was 10 cells/mL, and samples that were not processed in the cartridge showed no signal at all, as shown in Figure 4-3. With the sand samples, we were able to detect down to the lowest available concentration of seeded sample, 1000 cells per milliliter of sand, as shown in Figure 4-4. Note that the signal for the cartridge-processed sample has a significantly lower cycle threshold than the corresponding no-cartridge sample. We expect our LOD of vegetative cells from sand to be better than the 1000 cells per milliliter demonstrated here once the cartridges are tested at lower seeding levels.

Table 4-1 summarizes the results of these preliminary tests for the two-valve COTS-based AM cartridge, using either 5-mL liquid samples or 1-g sand samples mixed with 5 mL of water. The spores used were washed repeatedly to remove extraneous DNA. We will continue to test this cartridge version against a wider set of targets, including DNA from *Ba* culture supernatants, as well as other matrices of both environmental and clinical origin. For comparison, Table 4-1 also presents limits of detection for the same targets and matrices collected and processed using the LiNK (Lincoln Nucleic-acid Kit) 2.0 cartridge; note that the LiNK sample is much smaller in size.

Thus, we have tested the two-valve COTS-based AM cartridge on two matrices and have detected *Ba* spores and vegetative cells from samples up to the maximum design capacity of 5 mL of dirty water

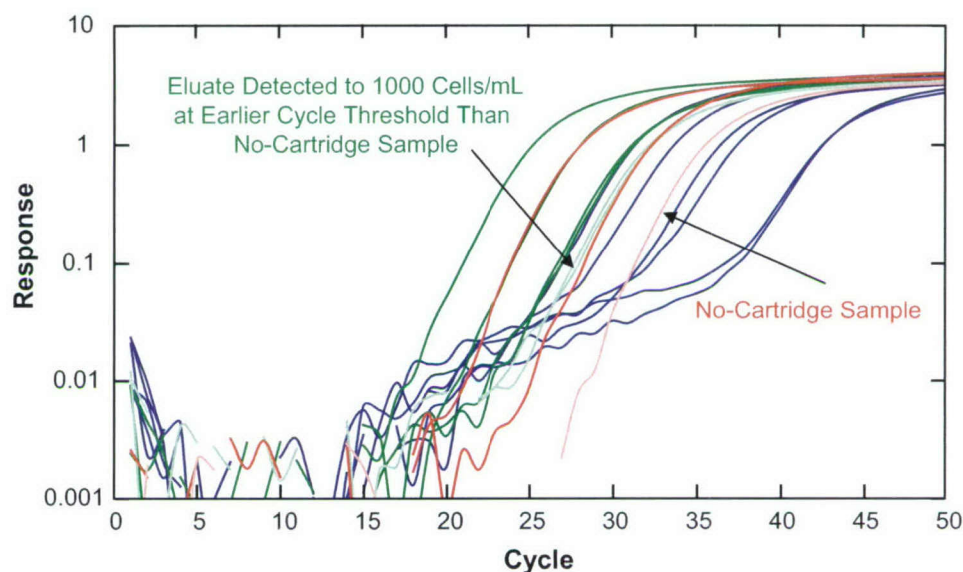


Figure 4-4. Detection of *Ba* vegetative cells seeded into sand using the AM cartridge protocol with a sample volume of 1 g of sand in 5 mL of distilled water, a magnetic bead mass of 15 mg, a two-cylinder-stack collection magnet in the processing chamber, and a magnetic bead collection time of 1 min. Detection is observed down to seeding levels of 1000 spores/mL at an earlier cycle threshold than with unprocessed samples. Note that this seeding level was the lowest tested in this experiment; we expect the limit of detection to be lower when lower levels are tested.

**TABLE 4-1**  
**Summary of Preliminary Test Results for COTS-Based AM Cartridge**

Target	Matrix	Number of Collection Magnets	Mass of Magnetic Beads (mg)	LOD (per mL)	Comment	LiNK 2.0 LOD (per mL)
Ba spore	Dirty water	10 spheres	25	10		1000
Ba spore	Sand	2 cylinders	15	100	Collection magnet in elution buffer	1000
Ba vegetative cell	Dirty water	2 cylinders	15	10		NA
Ba vegetative cell	Sand	2 cylinders	15	1000*	Expect lower LOD*	NA
*Lowest level tested so far.						



and 1 g of sand. Both of these sample volumes are substantially larger than the sample capacities of our lab-bench protocols, as well as larger than those of many commercially available sample preparation protocols for use in the laboratory. We have demonstrated that detection limits for both spores and vegetative cells are improved over those of samples subjected directly to PCR without concentration, and also that processing with the AM cartridge effectively removes PCR interferents.

L. Parameswaran

#### **REFERENCES**

1. Solid State Research Report, Lincoln Laboratory, MIT, 2004:4, p. 23.
2. Solid State Research Report, Lincoln Laboratory, MIT, 2001:4, p. 19.

## 5. ADVANCED IMAGING TECHNOLOGY

### 5.1 HIGH-FILL-FACTOR SILICON GEIGER-MODE AVALANCHE PHOTODIODE ARRAYS FOR PHOTON-COUNTING APPLICATIONS

Kilopixel Geiger-mode avalanche photodiode (GM-APD) arrays integrated with digital CMOS circuits have been successfully developed for laser radar (ladar) and photon-counting applications [1]. The GM-APD produces a digital detection signal in response to a single photon, which means that the signal is detected with quantum-limited sensitivity, and its time of arrival or incremental count is digitized in the pixel circuit, facilitating noiseless readout. Existing devices have low fill factors, necessitating microlenses or holographic spot projection to improve sensitivity. Unfortunately, many photon-counting applications require low  $f$ -numbers or small pixel dimensions so the detector sensitivity cannot be easily improved by applying optical techniques. We describe here ongoing work to increase the fill factor of silicon GM-APDs to near 100% at visible and near-infrared wavelengths.

Figure 5-1 shows a cartoon cross section of a conventional back-illuminated GM-APD pixel. A  $p^+$  buried layer acts as a field stop that is needed to create a high electric field (giving rise to an avalanche multiplier) within the region defined between the cathode and the  $p^+$  buried layer when the GM-APD is biased. In order to prevent edge breakdown, the  $p^+$  buried layer is recessed from the cathode perimeter. When the avalanche region is fully biased, the outer edge of the cathode, which has no field stop directly beneath it, depletes to the back side of the device, creating a nonavalanching absorber. Thus, photoelectrons collected in this region do not generate an avalanche event required to trigger the CMOS circuits. While this depletion region acts as a guard ring, preventing dark counts from being generated by surface leakage current, it also encroaches laterally into the active absorber. This effect reduces the fill factor, which can be a problem for small-diameter devices.

Several high-fill-factor GM-APD structures have been designed, fabricated, and characterized. Figure 5-2 shows a cartoon cross section of a successful GM-APD pixel structure that will be used as an example to describe the design approach. The pixel has a stepped  $p^+$  buried layer, where the layer adjacent to the cathode edge prevents depletion into the substrate. Because of the increased distance from the cathode, the electric field in this region is low. This prevents edge breakdown and surface-current-induced dark counts while significantly reducing nonavalanche photoelectron collection.

Figure 5-3 shows the processing steps used to create the stepped  $p^+$  buried layer. A lightly doped  $p$  epitaxial wafer ( $150\ \Omega\text{-cm}$  on  $p^+$ ) is used for starting material. An  $n$ -type arsenic cathode is formed by a masked implantation that is followed by a boron implant to create  $p$ -type channel stop isolation regions. An oxide is then patterned over the intended avalanche region, and a boron implant is performed, generating the shallow avalanche field stop under the oxide as well as the deeper cathode edge field stop everywhere else. Finally, the oxide is removed, and a metal contact is made to the cathode and substrate.

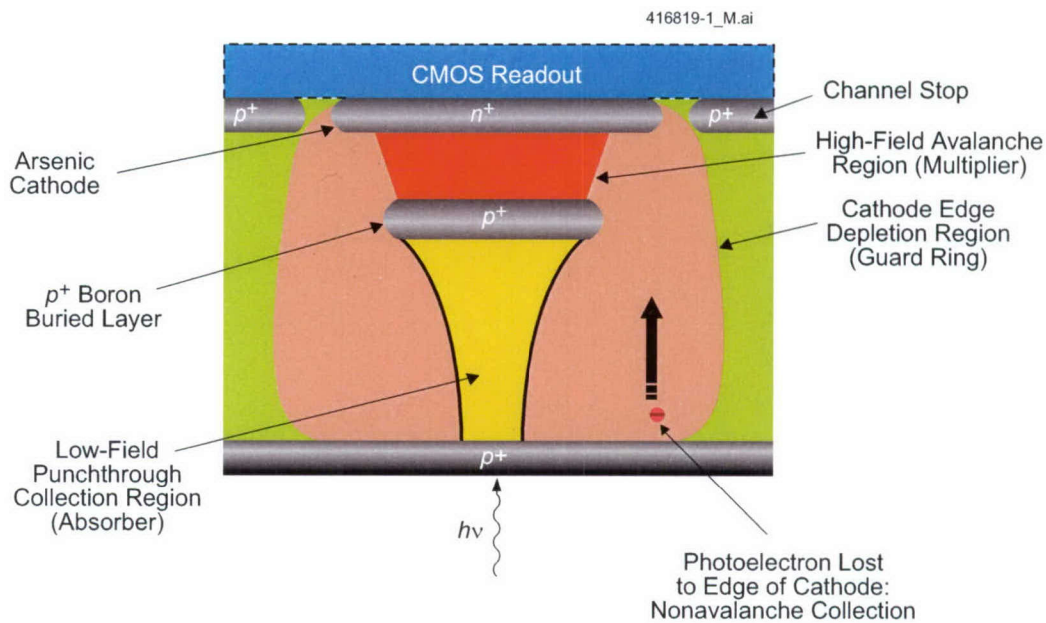


Figure 5-1. Cartoon cross section of traditional low-fill-factor Geiger-mode avalanche photodiode (GM-APD) showing avalanche region and guard ring.

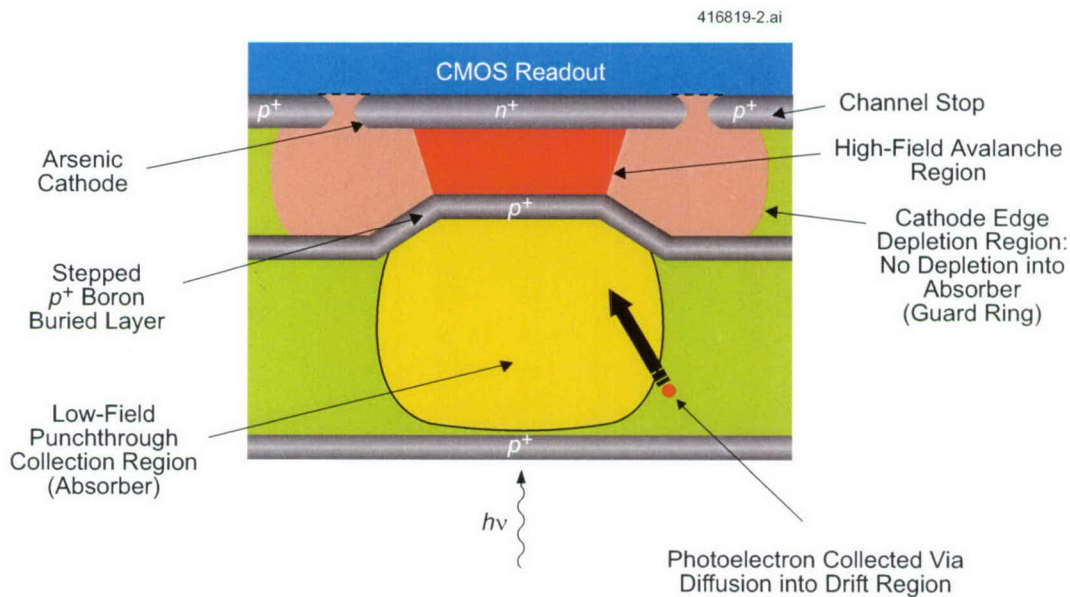


Figure 5-2. Cartoon cross section of high-fill-factor GM-APD showing avalanche region and guard ring.



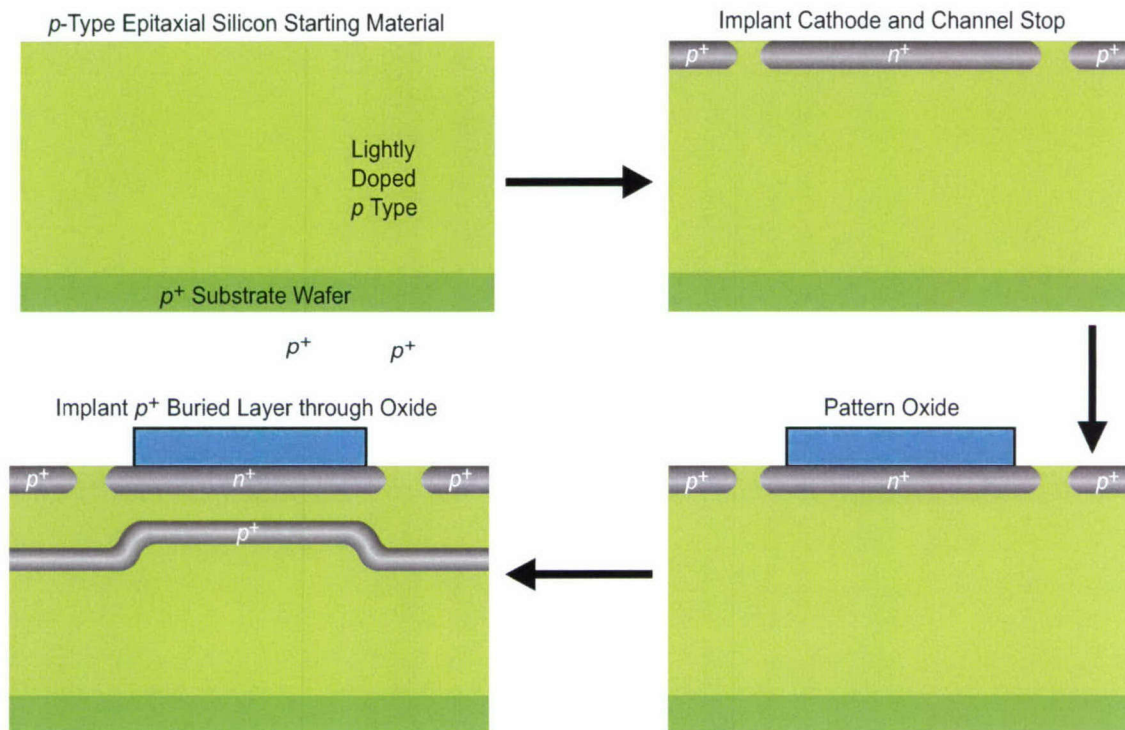


Figure 5-3. Process sequence to create high-fill-factor GM-APDs using a stepped  $p^+$  buried layer.

Constrained by a 5-V CMOS voltage swing, the shallow  $p^+$  buried layer is designed to allow high avalanche initiation probability and photoelectron collection efficiency when the APD is armed (5 V on cathode relative to the CMOS circuit ground), and to quench the device (drop the voltage below breakdown) and prevent afterpulsing (false counts caused by charge from a prior avalanche) when disarming (0 V on cathode relative to the CMOS circuit ground). As described below, the dose of the implant is varied to optimize the avalanche initiation probability and photoelectron collection efficiency. If the dose is too low, collection efficiency will be high but initiation probability poor; if the dose is too high, initiation probability will be good but collection efficiency poor.

To minimize the collection time and thus ladar range jitter, the conventional GM-APD is designed such that photoelectrons are collected by drift, rather than diffusion. To achieve this, the dose of the  $p^+$  buried layer is adjusted so that punchthrough and breakdown occur at approximately the same voltage. With a photon-counting device, where the response time is limited by quench time (tens of nanoseconds) and not transit time (hundreds of picoseconds), the  $p^+$  buried layer in the avalanche region is designed to have high initiation probability with relaxed collection times (although a reasonable collection efficiency is necessary to prevent image smear caused by photoelectron diffusion).

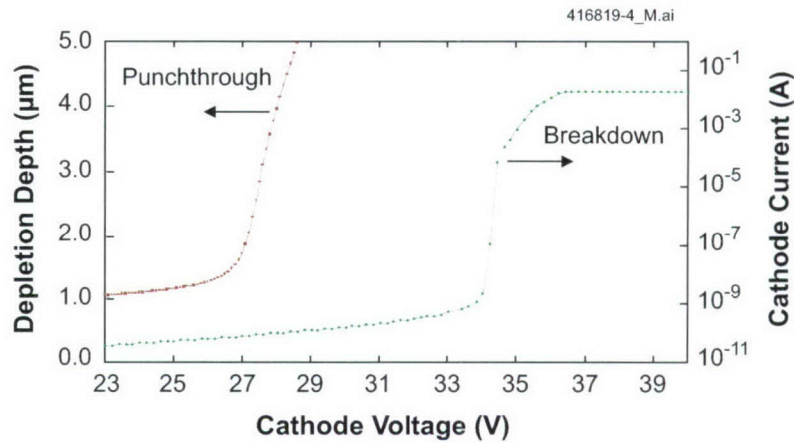


Figure 5-4. Breakdown and punchthrough values for GM-APD device at an implant dose of  $2.7 \times 10^{12} \text{ cm}^{-2}$ , showing punchthrough before breakdown, low initiation probability, and high collection efficiency.

The high-fill-factor device structure in Figure 5-3 was simulated using Silvaco computer-aided design tools (Athena for water processing, ATLAS for device operation). By using the data from existing ladar devices to calibrate the Silvaco simulations, breakdown and punchthrough estimates were extracted to determine the optimum  $p^+$  buried layer dose for the high-field avalanche region. Based on previous ladar device simulations and measured results, a shallow field stop depth of  $\sim 0.6 \text{ } \mu\text{m}$  was used, as this condition gives a low breakdown voltage ( $\sim 30 \text{ V}$ ) while having negligible tunneling currents. Simulations showed a boron implant energy of 675 keV (near the upper limit of easily obtained and commercially available implant energies), and a dose of  $\sim 2.8 \times 10^{12} \text{ cm}^{-2}$  provided good initiation probability and collection efficiency in the avalanche region without breakdown or punchthrough occurring at the cathode edge. The results indicate a narrow implant dose range of  $\sim 10\%$  to operate well within the 5-V CMOS voltage swing.

To evaluate the  $p^+$  buried layer dose, six wafers were fabricated with the following doses: one wafer at  $2.5 \times 10^{12} \text{ cm}^{-2}$ , two wafers at  $2.7 \times 10^{12} \text{ cm}^{-2}$ , two wafers at  $2.9 \times 10^{12} \text{ cm}^{-2}$ , and one wafer at  $3.1 \times 10^{12} \text{ cm}^{-2}$ . The expectation from simulations was that punchthrough and breakdown voltages would coincide at a dose between  $2.7 \times 10^{12} \text{ cm}^{-2}$  and  $2.9 \times 10^{12} \text{ cm}^{-2}$ .

The GM-APD breakdown voltage values were estimated from current-voltage (I-V) curves, and the punchthrough voltages were from capacitance voltage (C-V) measurements. Figure 5-4 ( $2.7 \times 10^{12} \text{ cm}^{-2}$ ) shows punchthrough occurring below the breakdown voltage, whereas Figure 5-5 ( $2.9 \times 10^{12} \text{ cm}^{-2}$ ) shows a reversal in the voltage values. Therefore, the breakdown and punchthrough voltages should coincide for a device at a dose of  $\sim 2.8 \times 10^{12} \text{ cm}^{-2}$ . Simulations show a punchthrough at 2 V above breakdown for a dose of  $2.9 \times 10^{12} \text{ cm}^{-2}$ , indicating good initiation probability and collection efficiency for a photon-counting application.



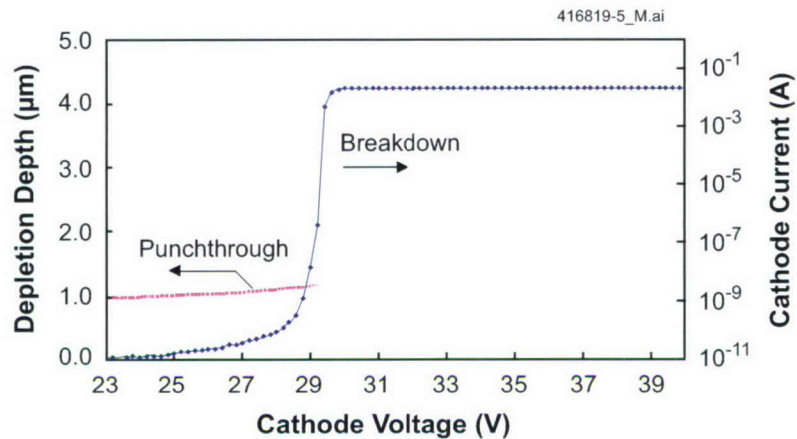


Figure 5-5. Breakdown and punchthrough values for GM-APD device at an implant dose of  $2.9 \times 10^{12} \text{ cm}^{-2}$ , showing breakdown before punchthrough resulting in a higher initiation probability and lower collection efficiency than in Figure 5-4.

Future work on the high-fill-factor GM-APDs includes more detailed characterization of device operation, and process development to improve performance. Front-illuminated devices will be used to characterize ionization probability and collection efficiency. To measure the fill factor, dark counts, and other detector characteristics, the GM-APDs will need to be bonded to CMOS readout circuits and processed through back illumination. As the dimensions of the high-fill-factor pixel are reduced, crosstalk, a process by which photons generated by the hot avalanche electrons are absorbed by adjacent pixels, will increase; the extent of crosstalk must be carefully measured. To reduce the crosstalk, a process is being developed that uses filled trenches between the GM-APDs.

The early results on high-fill-factor silicon GM-APD designs are promising, with successful demonstration of breakdown and punchthrough characteristics. These detectors will increase the range of applications in the growing field of single-photon-sensitive APD arrays.

M. J. Renzi	B. F. Aull
B. B. Kosicki	R. K. Reich
D. J. Young	

## REFERENCE

1. R. Heinrichs, B. F. Aull, R. M. Marino, D. G. Fouche, A. K. McIntosh, J. J. Zayhowski, T. Stephens, M. E. O'Brien, and M. A. Albota, *Proc. SPIE* **4377**, 106 (2001).



## 6. ANALOG DEVICE TECHNOLOGY

### 6.1 INTERMODULATION DISTORTION IN HIGH-TEMPERATURE SUPERCONDUCTOR FILTERS

In high-temperature superconductor (HTS) filters and delay lines, nonlinear behavior limits the performance because of intermodulation distortion (IMD) generated. It limits the dynamic range of receive filters and thus is important even in low-power applications of HTS filters. Filters with large numbers of poles or with very narrow bandwidths are the most sensitive to the IMD. It is desirable to be able to predict the IMD in a given filter when the characteristics of the film used to fabricate the filter are known. We have successfully modeled the IMD in a resonator using the nonlinear  $Z_S$  and extended the modeling to a resonator-coupled filter.

The IMD in a resonator is generated by the same processes that are responsible for the nonlinear surface impedance  $Z_S$ , given by  $Z_S(I) = R_S(I) + j\omega\mu_0\lambda(I)$ , where  $I$  is the total rf current in the resonator. Thus, the IMD can be derived from the  $Z_S$ . A superconducting resonator can be modeled by the equivalent circuit shown in Figure 6-1, where the component values are given in [1]. It has been demonstrated that the nonlinear inductance can be modeled by

$$L = L_0 + L_2 I^2 \quad (6.1)$$

and the nonlinear resistance by

$$R = R_0 - R_2 I^2 \quad (6.2)$$

where  $L_2$  is a constant proportional to the nonlinear part of the penetration depth, and  $R_2$  is the nonlinear part of  $R$ , related to the nonlinear surface resistance.

We have derived resonator IMD from  $Z_S(P)$ , where  $P$  is the input power and is related to  $I$  [1]. As a verification that the IMD results from the nonlinear surface impedance, we have used the measured changes in center frequency  $f_0(P)$  and  $Q(P)$  of a YBCO resonator along with the equivalent circuit of Figure 6-1 to calculate the IMD generated. We have used the harmonic balance [2] procedure in a computer-aided design (CAD) tool package to carry out the calculations [3] to compare with the measured IMD. We have assumed an inductance and resistance with the functional form given in Equations (6.1) and (6.2). The  $L_2$  and  $R_2$  were determined by a fit to the measured  $f_0(P)$  and  $Q(P)$  data using the equivalent circuit and the CAD package.

The result of the IMD calculation is shown in Figure 6-2, which plots input power vs the measured and calculated values of output power at the fundamental frequency of the resonator and the measured and calculated values of output power of one of the third-order IMD tones. There are no further free parameters

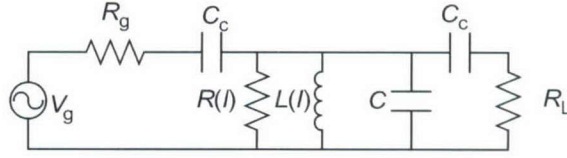


Figure 6-1. Equivalent circuit of a resonator.  $R(I)$  and  $L(I)$  are from Equations (6.1) and (6.2), where  $R_0$ ,  $L_0$ , and  $C$  are given by the transmission line parameters [1].  $C_c$  is the coupling capacitor, and  $R_g = R_L = 50 \, \Omega$  are the load and source impedances. The resonator  $Q$  is given by  $R/\omega L$ .

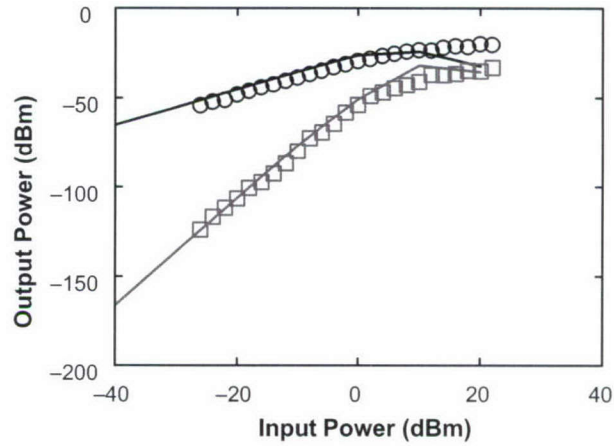


Figure 6-2. Measured and calculated intermodulation distortion (IMD) for YBCO resonator at  $T = 50 \, \text{K}$ . Solid lines are calculations, open circles are the measured fundamental frequency, and open squares are the measured third-order IMD.

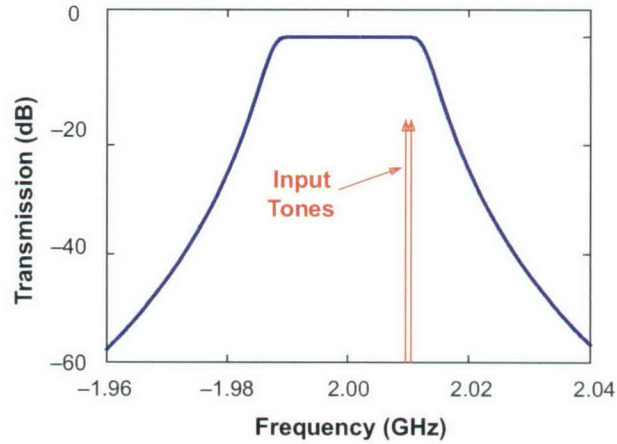


Figure 6-3. Frequency response of five-pole filter and position of input tones for the intermodulation calculation. The frequencies are 2.0095 and 2.0105 GHz, chosen to be centered at the edge of the passband.

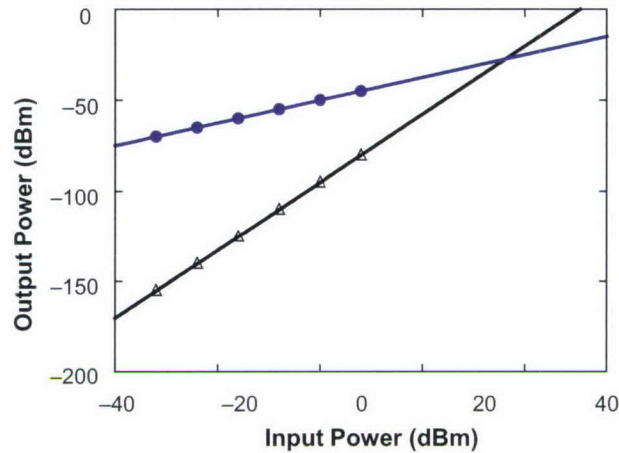


Figure 6-4. Results of the intermodulation calculation. Circles are the output at fundamental frequencies, and triangles are the output at intermodulation frequencies.

in the fitting. The agreement is excellent, verifying that the IMD can be derived from the nonlinear surface impedance. In this measurement the IMD depends on the third power of the input power, as seen by the slope of three in the double logarithmic plot. This is not always the case. The calculation, because of the assumptions of the quadratic dependence of  $R$  and  $L$  on current, can only yield a cubic dependence on power. Not all cases will yield such good agreement between this model and experiment. In many experiments the slope is smaller than three. Also, because  $L_2$  and  $R_2$  are determined from the fit of the measured data, they are the appropriate parameters for relatively high power and thus might not yield a good fit to the IMD at low power in all cases. We used measurements at a temperature of 50 K for these calculations because the high-power and low-power nonlinearities could be fit with the same parameters.

Since the resonator results have verified that this is an accurate model of IMD, we have also used the resonator results to extend the IMD modeling to a bandpass filter. As a typical HTS filter, we chose a five-pole design with center frequency of 2 GHz and 1% fractional bandwidth. The filter was modeled as five capacitively coupled resonators, each with the equivalent circuit of Figure 6-1. The  $L_0$  and  $C_0$  of each of the resonators were chosen to give a Chebyshev response at low power, shown in Figure 6-3. Included in the linear response is the finite  $Q$  of the resonator. The nonlinear parameters were the same as used for the simulation of the single-resonator IMD. Also shown in Figure 6-3 is the position of the two simulated tones used to generate the IMD. The tones were located at the edge of the passband, because the resonator currents are highest at that frequency and therefore the IMD is higher than when the tones are located at midband.

The results of the harmonic balance simulation of the filter are shown in Figure 6-4. The intermodulation power at +10-dBm input power to the filter is ~70 dB below the input. This simulation should be understood as an approximate calculation for a real filter because the results obviously depend



on the geometry of the resonators. However, the stripline geometry, with  $\sim 30\text{-}\Omega$  impedance resonators as used here, is already one with only moderate current crowding and therefore moderate nonlinearities.

Geometrical mitigation of nonlinearities will not produce dramatic improvements in the IMD performance. Filters with narrower bandwidths or with more poles will produce an even higher level of IMD. Also, it should be noted that the nonlinear parameters used for this simulation have been extracted from a very high quality YBCO film that has been shown to exhibit nonlinearities that agree with the intrinsic limit imposed by the d-wave symmetry of the order parameter in the HTS materials [4],[5]. The level of IMD shown in Figure 6-4 may be too high for some applications that require very high dynamic range.

D. E. Oates

### REFERENCES

1. D. E. Oates, A. C. Anderson, and P. M. Mankiewich, *J. Supercond.* **3**, 251 (1990).
2. S. A. Maas, *Nonlinear Microwave Circuits* (IEEE, Piscataway, NJ, 1997), Chap. 3.
3. Advanced Design System, Agilent Technologies.
4. D. E. Oates, S.-H. Park, and G. Koren, *Phys. Rev. Lett.* **93**, 197001-1 (2004).
5. D. E. Oates, S.-H. Park, D. Agassi, G. Koren, and K. Irgmaier, to be published in *IEEE Trans. Appl. Supercond.*, 2005.

## 7. ADVANCED SILICON TECHNOLOGY

### 7.1 MEGAPIXEL CMOS IMAGE SENSOR FABRICATED IN THREE-DIMENSIONAL INTEGRATED CIRCUIT TECHNOLOGY

Dense, vertical interconnection of integrated circuits—three-dimensional (3-D) technology—can relax power, performance, and computational trade-offs inherent to conventional planar circuit topologies. Active pixel focal plane architectures are well suited for 3-D interconnection because signal integration, amplification, and readout can be in close proximity to the photodetection elements while still achieving 100% optical fill factor. The further capability to perform complex signal processing behind every pixel can dramatically reduce total image sensor power and bandwidth requirements. Flip-chip hybrid stacks of independently optimized photodetector and readout multiplexer designs can achieve scientific-grade image sensor performance [1]. However, these bump-bonded hybrid approaches are limited to two circuit layers and to large pixel sizes ( $\geq 18\ \mu\text{m}$ ), and they do not permit postintegration hydrogen passivation anneals, which are critical for dark current suppression.

We have developed a 3-D integration method that is extendable to three or more circuit layers and is capable of achieving far smaller pixel sizes than possible with bump bonding. Earlier, we demonstrated a  $64 \times 64$ ,  $12\text{-}\mu\text{m}$ -pixel active pixel sensor with per-pixel analog-to-digital conversion using  $0.8\text{-}\mu\text{m}$ -gate-length silicon-on-insulator (SOI) CMOS, epoxy adhesive bonding, and  $6\text{-}\mu\text{m}$ -diameter 3-D vias [2]. To accommodate the higher temperatures ( $400\text{--}475^\circ\text{C}$ ) required for via plug fill and defect state hydrogenation, a CMOS-compatible oxide-to-oxide wafer bonding process was developed and used to demonstrate via chains through three circuit layers and ring oscillators through two circuit layers [3].

Here, we present a 3-D integrated  $1024 \times 1024$ ,  $8\text{-}\mu\text{m}$ -pixel visible image sensor fabricated with oxide-to-oxide wafer bonding and  $2\text{-}\mu\text{m}$ -square 3-D vias in every pixel. The 150-mm wafer technology integrates a low-leakage, deep-depletion, 100% fill factor photodiode layer to a 3.3-V,  $0.35\text{-}\mu\text{m}$ -gate-length fully depleted (FD) SOI CMOS readout circuit layer.

Photodiodes and CMOS pixel electronics were fabricated in two separate 150-mm circuit wafer lots and assembled into a 3-D stack, shown schematically in Figure 7-1. Each circuit layer of the 3-D stack is referred to as a tier. The photodiode tier (tier 1) consisted of  $p^+n$  diodes in high-resistivity ( $>3000\ \Omega\text{-cm}$ ,  $n$  type) float-zone silicon substrates. The diode's lateral doping profile is graded using implant masking and thermal annealing to minimize the surface contribution to dark current. A standard planar CMOS back-end sequence forms contact, plugs, and a metal layer. The second tier (tier 2) is fabricated using our  $0.35\text{-}\mu\text{m}$  FDSOI CMOS process with  $7.2\text{-nm}$  gate oxide, cobalt silicide, and planar three-level-metal interconnect.

After completion of individual circuit tier fabrication, tier 2 is inverted over tier 1, aligned, and mated using a low-temperature oxide-oxide bonding process [3]. A wet chemical etch removes the tier-2 handle wafer down to the buried oxide. A multistep dry etch process forms  $2\text{-}\mu\text{m}$ -square 3-D vias between



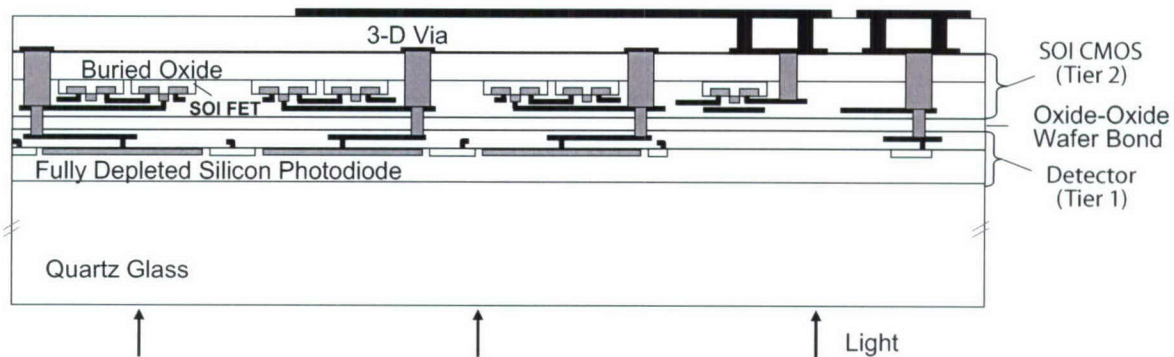


Figure 7-1. Schematic diagram of three-dimensional (3-D) stacked imager circuit. Tier 1 is a silicon photodetector wafer, and tier 2 is an inverted fully depleted silicon-on-insulator (FDSOI) CMOS wafer.

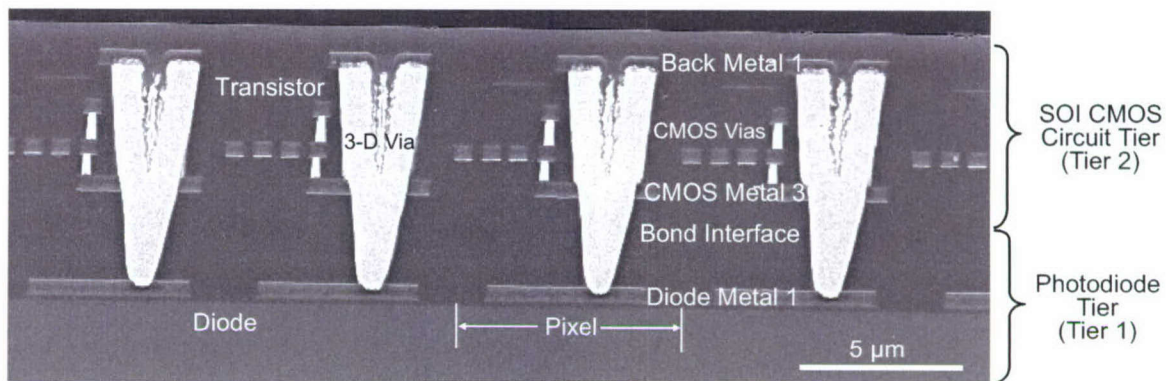


Figure 7-2. Cross-sectional scanning electron micrograph through a functional active pixel imager.

tier 2 and tier 1. The  $\sim 7.5\text{-}\mu\text{m}$  via depth is filled with Ti/TiN liner deposited from a collimated bias-sputter source, tungsten (W) plugs are formed by chemical vapor deposition ( $475^\circ\text{C}$ ) to connect the two metal layers, and excess metal is removed by chemical-mechanical planarization. At this point additional tiers could be bonded and interconnected. To prepare the 3-D stack for illumination from the photodiode side, the detector tier silicon is thinned to  $\sim 50\text{ }\mu\text{m}$ , coated with an antireflection layer, and then mounted onto a transparent support in a process sequence similar to that used to make back-illuminated charge-coupled devices [4]. Standard semiconductor equipment was used for all processing steps.

A cross-sectional scanning electron micrograph (SEM) through several  $8\text{-}\mu\text{m}$  pixels of a functional active pixel imager is shown in Figure 7-2. The oxide-oxide bond between the two tiers is imperceptible. A 3-D via connects tier-2 FDSOI CMOS metal 3 to tier-1 (diode) metal 1, and a metal cap (back metal 1) covers the 3-D via plug. The  $50\text{-nm}$ -thick SOI transistor features can be seen near the top of the SEM. The dominant misalignment ( $\sim 1\text{ }\mu\text{m}$ ) is created by the wafer-to-wafer bonding step.



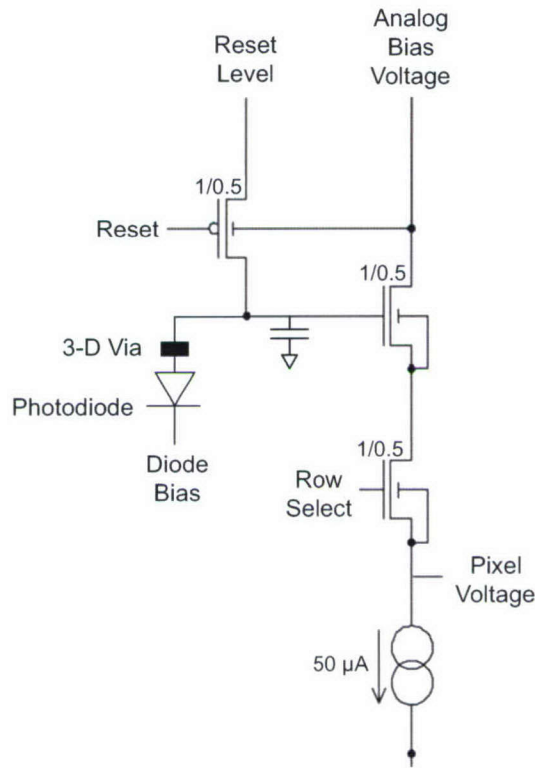


Figure 7-3. Schematic of a pixel of the  $1024 \times 1024$  array. Each pixel includes a reverse-biased  $p^+/n$  diode (in tier 1) and a reset transistor, source follower transistor, and select transistor (in tier 2).

Figure 7-3 shows a pixel schematic. Each pixel of the  $1024 \times 1024$  array includes a reverse-biased  $p^+/n$  diode (in tier 1) and a reset transistor, source follower transistor, and select transistor (in tier 2). Two principal imager design variations were included on the mask set: a  $p$ -MOS reset transistor with additional in-pixel capacitance to support a larger dynamic range, and an  $n$ -MOS reset transistor for lower-light-level imaging. Figure 7-4 shows photographs of the 150-mm wafer and the  $22 \times 22$ -mm die after 3-D integration. A block diagram of the imager is shown in Figure 7-5. The sensor operates in a rolling shutter configuration with row select, row integration reset, and column select each controlled by a token-loaded shift register. After 3-D integration, functional  $p$ -MOS reset and  $n$ -MOS reset imagers were both evaluated with timing and analog-to-digital conversion occurring off chip.

Pixel responsivity and dynamic range were close to design expectations. Measured responsivity from the  $p$ -MOS reset imager with added in-pixel capacitance was  $\sim 2.7 \mu\text{V}/e^-$  and from the  $n$ -MOS reset imager was  $\sim 9.4 \mu\text{V}/e^-$ , corresponding to a charge-handling capacity of 350,000  $e^-$  and 85,000  $e^-$ , respectively. The  $p$ -MOS reset design has the added feature of blooming control, which was successfully tested to  $5\times$  the saturation level.

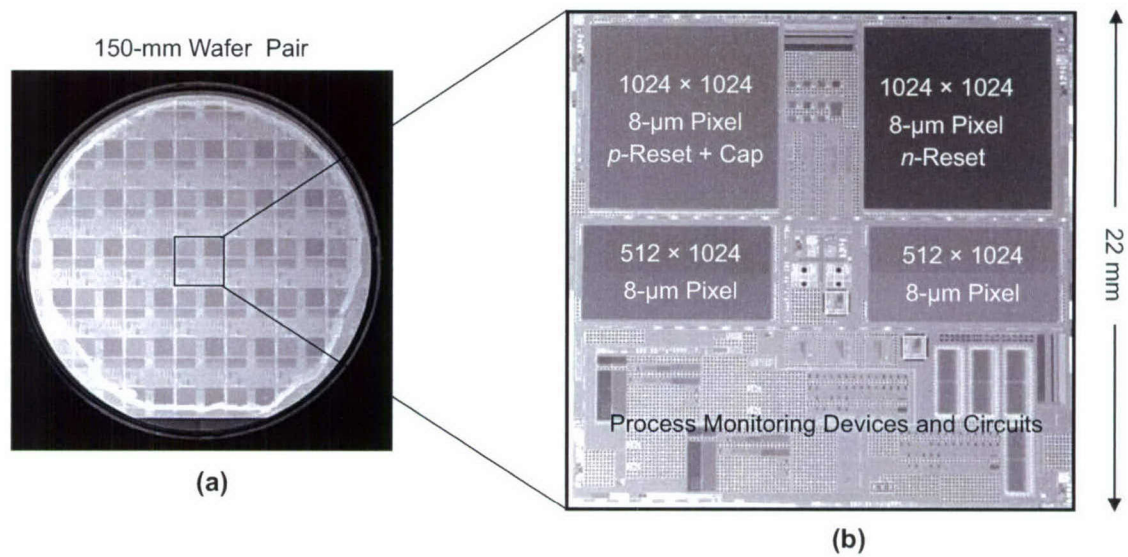


Figure 7-4. Photographs of (a) completed 3-D integrated 150-mm wafer pair and (b) 22 × 22-mm die after integration.

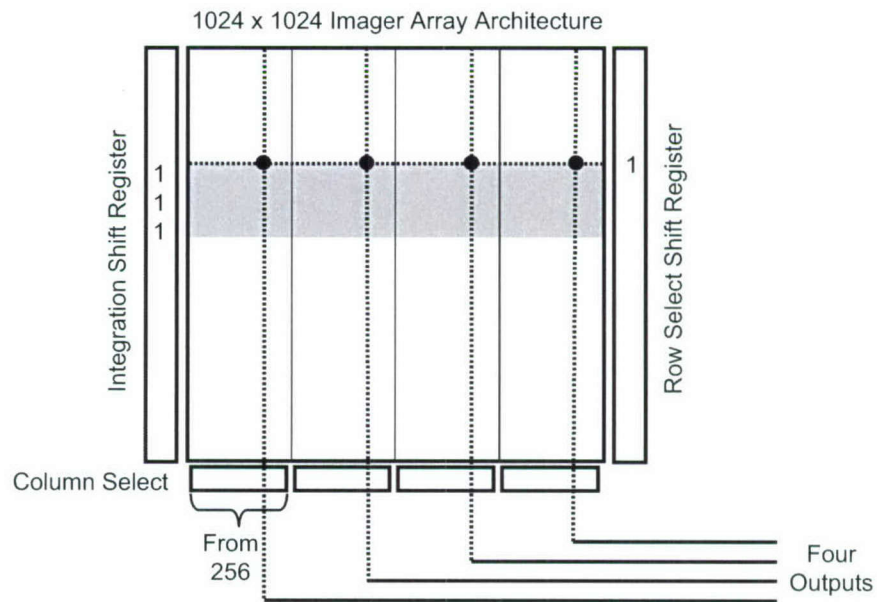


Figure 7-5. Block diagram of 3-D integrated image sensor.

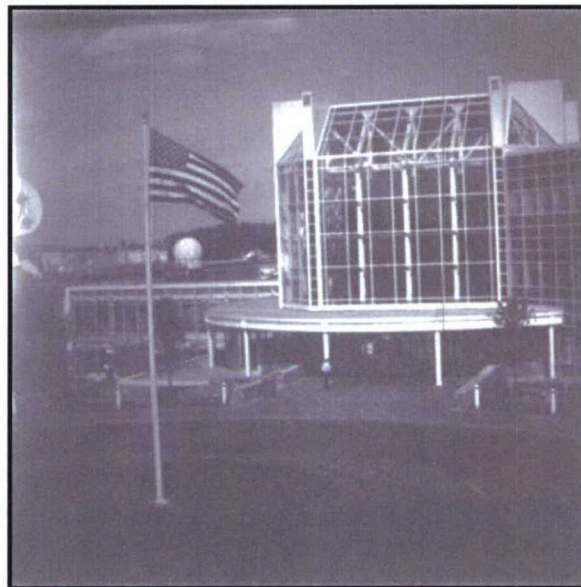


Figure 7-6. Sample image from the  $1024 \times 1024$ -pixel array.

Each sensor contained over 3.8 million transistors and over one million 3-D vias. We measured pixel operability in excess of 99.9% with the principal yield detractor arising from column or row dropouts (i.e., not 3-D vias). Single-tier photodiodes exhibited dark current of  $<0.2 \text{ nA/cm}^2$ . On 3-D imagers with full thickness ( $675 \text{ }\mu\text{m}$ ) diodes, we measured room-temperature detector dark current at  $1\text{--}3 \text{ nA/cm}^2$ . Additional sintering and full-depletion back-illuminated processing are expected to produce a  $10\text{--}100\times$  reduction in dark current. The high degree of pixel functionality can be seen in Figure 7-6, which presents an image acquired by projecting a 35-mm slide onto the CMOS-circuit side of the 3-D integrated imager.

V. Suntharalingam	R. Berger	J. A. Burns
C. K. Chen	C. L. Keast	J. M. Knecht
R. D. Lambert	K. L. Newcomb	D. M. O'Mara
D. D. Rathman	D. C. Shaver	A. M. Soares
C. N. Stevenson	B. M. Tyrrell	K. Warner
B. D. Wheeler	D.-R. W. Yost	D. J. Young

## REFERENCES

1. Y. Bai, S. G. Bernd, J. R. Hosack, M. C. Farris, J. T. Montroy, and J. Bajaj, *Proc. SPIE* **5167**, 83 (2004).



2. J. Burns, C. L. Keast, P. W. Wyatt, K. Warner, A. Loomis, L. McGrath, and C. Lewis, *International Solid-State Circuits Conference Digest of Technical Papers* (IEEE, Piscataway, NJ, 2001), p. 268.
3. K. Warner, W. Mowers, J. A. Burns, D. Lennon, C. L. Keast, D. R. Yost, A. Loomis, and R. Kunz, *Proceedings of the International SOI Conference* (IEEE, Piscataway, NJ, 2002), p. 123.
4. B. E. Burke, J. A. Gregory, M. W. Bautz, G. Y. Prigozhin, S. E. Kissel, B. B. Kosicki, A. H. Loomis, and D. J. Young, *IEEE Trans. Electron Devices* **44**, 1633 (1997).

REPORT DOCUMENTATION PAGE				Form Approved OMB No. 0704-0188																	
Public reporting burden for this collection of information is estimated to average 1 hour per response, including the time for reviewing instructions, searching existing data sources, gathering and maintaining the data needed, and completing and reviewing this collection of information. Send comments regarding this burden estimate or any other aspect of this collection of information, including suggestions for reducing this burden to Department of Defense, Washington Headquarters Services, Directorate for Information Operations and Reports (0704-0188), 1215 Jefferson Davis Highway, Suite 1204, Arlington, VA 22202-4302. Respondents should be aware that notwithstanding any other provision of law, no person shall be subject to any penalty for failing to comply with a collection of information if it does not display a currently valid OMB control number. <b>PLEASE DO NOT RETURN YOUR FORM TO THE ABOVE ADDRESS.</b>																					
1. REPORT DATE (DD-MM-YYYY) 15-02-2005		2. REPORT TYPE Quarterly Technical Report		3. DATES COVERED (From - To) 1 November 2004 – 31 January 2005																	
4. TITLE AND SUBTITLE  Solid State Research				5a. CONTRACT NUMBER F19628-00-C-0002																	
				5b. GRANT NUMBER																	
				5c. PROGRAM ELEMENT NUMBER																	
6. AUTHOR(S)  David C. Shaver				5d. PROJECT NUMBER 221																	
				5e. TASK NUMBER 961																	
				5f. WORK UNIT NUMBER																	
7. PERFORMING ORGANIZATION NAME(S) AND ADDRESS(ES)  Lincoln Laboratory, MIT 244 Wood Street Lexington, MA 02420-9108				8. PERFORMING ORGANIZATION REPORT NUMBER  2005:1																	
9. SPONSORING / MONITORING AGENCY NAME(S) AND ADDRESS(ES)  HQ Air Force Materiel Command AFMC/STSC Wright-Patterson AFB, OH 45433-5001				10. SPONSOR/MONITOR'S ACRONYM(S)																	
				11. SPONSOR/MONITOR'S REPORT NUMBER(S) ESC-TR-2005-058																	
12. DISTRIBUTION / AVAILABILITY STATEMENT  Approved for public release; distribution is unlimited.																					
13. SUPPLEMENTARY NOTES None																					
14. ABSTRACT  This report covers in detail the research work of the Solid State Division at Lincoln Laboratory for the period 1 November 2004 through 31 January 2005. The topics covered are Quantum Electronics, Electro-optical Materials and Devices, Submicrometer Technology, Biosensor and Molecular Technologies, Advanced Imaging Technology, Analog Device Technology, and Advanced Silicon Technology. Funding is provided by several DoD organizations—including the Air Force, Army, DARPA, MDA, Navy, NSA, and OSD—and also by the DOE, NASA, and NIST.																					
15. SUBJECT TERMS <table border="0"> <tr> <td>quantum electronics</td> <td>biosensor technology</td> <td>bioaerosol detection</td> <td>avalanche photodiode arrays</td> </tr> <tr> <td>electro-optical devices</td> <td>molecular technology</td> <td>external-cavity lasers</td> <td>high-temperature superconductors</td> </tr> <tr> <td>materials research</td> <td>advanced imaging technology</td> <td>variable apodizers</td> <td>3-D integrated circuit technology</td> </tr> <tr> <td>submicrometer technology</td> <td>analog device technology</td> <td>DNA analysis</td> <td></td> </tr> </table>						quantum electronics	biosensor technology	bioaerosol detection	avalanche photodiode arrays	electro-optical devices	molecular technology	external-cavity lasers	high-temperature superconductors	materials research	advanced imaging technology	variable apodizers	3-D integrated circuit technology	submicrometer technology	analog device technology	DNA analysis	
quantum electronics	biosensor technology	bioaerosol detection	avalanche photodiode arrays																		
electro-optical devices	molecular technology	external-cavity lasers	high-temperature superconductors																		
materials research	advanced imaging technology	variable apodizers	3-D integrated circuit technology																		
submicrometer technology	analog device technology	DNA analysis																			
16. SECURITY CLASSIFICATION OF:			17. LIMITATION OF ABSTRACT  None	18. NUMBER OF PAGES  68	19a. NAME OF RESPONSIBLE PERSON																
a. REPORT Unclassified	b. ABSTRACT Same as report	c. THIS PAGE Same as report			19b. TELEPHONE NUMBER (include area code)																